CHAPTER 1:

Detector Performance

In this chapter. . .

1.1 Overview

ACS employs two fundamentally different types of detectors: CCDs for use from the near-UV to the near-IR, and a Multi-Anode Microchannel Array detector known as a MAMA for use in the ultraviolet. The CCD and the MAMA detectors are used in different ways and impose their own unique limitations on the feasibility of observations performed with them. This chapter covers the properties of the ACS detectors, descriptions of how to use them to optimize scientific programs, and steps needed to ensure the feasibility of observations.

1.2 The CCDs

1.2.1 Detector Properties

WFC Properties

The WFC/CCD consists of two 4096 x 2048 charge-coupled devices that are sensitive from the near-UV to the near-IR. These CCDs are

thinned, backside-illuminated devices manufactured by Scientific Imaging Technologies (SITe) and are butted together along their long dimension to create an effective 4096×4096 array with a gap corresponding to approximately 50 pixels between the chips. The CCD camera design incorporates a warm dewar window, designed to prevent buildup of contaminants on the window that cause a loss of UV throughput.

A summary of the ACS CCD performance is given in Table 3.1.

HRC

The HRC CCD is a flight-spare STIS 1024×1024 CCD and is a thinned, backside-illuminated device, manufactured at SITe. The coating uses a process developed by SITe to provide good quantum efficiency in the near-ultraviolet. The performance characteristics and specifications are given in Table 3.1

1.2.2 CCD Spectral Response

The responsive quantum efficiency (RQE) of the WFC and HRC CCDs is shown in Figure 1.1; the RQE includes corrections needed to reproduce the instrument sensitivity measured on orbit (ACS ISR 2007-06). The total spectral response of the camera (see Figure 2.7) is given by the convolution of the RQEs shown here and the throughput of optical elements of the camera. For example, the WFC silver coated mirrors enhance the reflectivity in the near-IR but impose a violet cutoff below 370nm.

Figure 1.1: Responsive quantum efficiency of the HRC CCD (solid line) and WFC CCDs (dashed line).

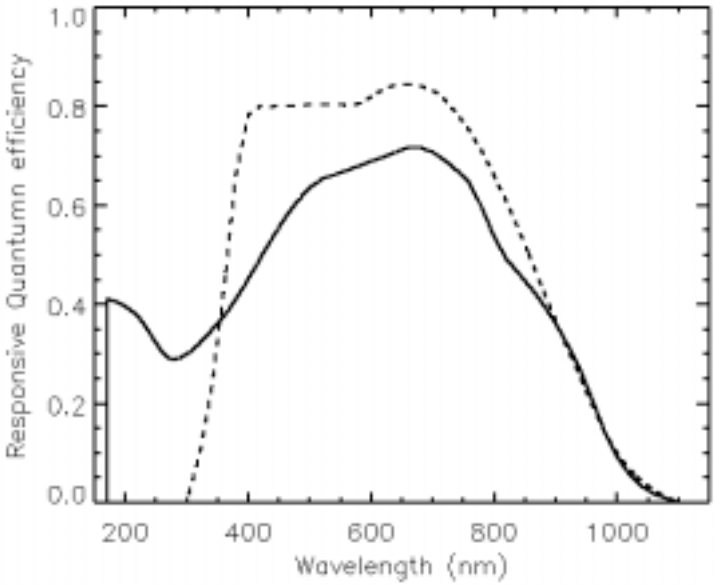

1.2.3 Quantum Efficiency Hysteresis

Based on current data, the ACS CCDs do not suffer from quantum efficiency hysteresis (QEH). The CCDs respond in the same way to light levels over their whole dynamic range, irrespective of the previous illumination level.

1.2.4 CCD Long-Wavelength Fringing

Like most thinned CCDs, the ACS CCDs exhibit fringing in the red, longward of ~7500 Å. The amplitude of the fringes is a strong function of wavelength and spectral resolution. The fringe pattern can be corrected by rectification with an appropriate flat field. The fringe pattern is a convolution of the contours of constant distance between the front and back surfaces of the CCD, and the wavelength of light on a particular part of the CCD. The fringe pattern has been shown to be very stable in similar devices, as long as the wavelength of light on a particular part of the CCD stays constant. In practice, this means that the fringe pattern is dependent on the spectrum of the light incident on the detector, with the sensitivity to the source spectrum a function of the bandwidth of the filter.

1.2.5 Readout Format

WFC

Each CCD chip is read out as a 4144×2068 array, including physical and virtual overscans. Two different amplifiers are used to read out each half of the chip. The final images consist of 24 columns of physical overscan, 4096 columns of pixel data, and another 24 columns of physical overscan. Each column consists of 2048 rows of pixel data followed by 20 rows of virtual overscan. The orientation of the chip is such that for the grism spectra, the dispersed images have wavelength increasing from left to right in the positive x-direction.

HRC

The HRC CCD is read out as a 1062×1044 array, including physical and virtual overscans. There are 19 columns of physical overscan, followed by 1024 columns of pixel data, and then 19 more columns of physical overscan. Each column consists of 1024 rows of pixel data followed by 20 rows of virtual overscan. As with the WFC, the orientation of the chip was chosen so that grism images have wavelength increasing from left to right.

1.2.6 Analog-To-Digital Conversion

Electrons which accumulate in the CCD wells are read out and converted to data numbers (DN) by the analog-to-digital converter (ADC). The ADC output is a 16 bit number, producing a maximum of 65,535 DN in one pixel.

Up to Cycle 15 the CCDs were capable of operating at gains of 1, 2, 4 or 8 electrons/DN. While for the HRC operation no changes are expected for Cycle 17, the possible gain settings for the WFC are still to be defined. In principle, use of a lower gain value can increase the dynamic range of faint source observations by reducing the quantization noise; however, in practice this improvement is not significant. Table 1.1 and Table 1.2 show the actual gain levels and readout noise in electrons for the four WFC amps, and the default C amp used for the HRC for SIDE 1 and SIDE 2 respectively.

Table 1.1: CCD gain and readout noise (e^- rms) under SIDE-1 operation (03/2002->06/2006).

		Gain=1		Gain=2 (default)		Gain=4	
Chip	**Amp**	**Gain**	**Noise**	**Gain**	**Noise**	**Gain**	**Noise**
WFC1	A	1.000	5.57	2.002	5.84	4.01	- - -
WFC1	B	0.972	4.70	1.945	4.98	3.90	- - -
WFC2	C	1.011	5.18	2.028	5.35	4.07	- - -
WFC2	D	1.018	4.80	1.994	5.27	4.00	- - -
HRC	C	1.163	4.46	2.216	4.80	4.235	5.86

Table 1.2: CCD gain and readout noise (e^- rms) under SIDE-2 operation (07/2006-01/2008)

		Gain=1		Gain=2 (default)		Gain=4	
Chip	**Amp**	**Gain**	**Noise**	**Gain**	**Noise**	**Gain**	**Noise**
WFC1	A	1.000	5.29	2.002	5.62	4.01	- - -
WFC1	B	0.972	4.45	1.945	4.74	3.90	- - -
WFC2	C	1.011	5.03	2.028	5.34	4.07	- - -
WFC2	D	1.018	4.55	1.994	4.89	4.00	- - -
HRC	C	1.163	4.36	2.216	4.82	4.235	5.44

As in previous cycles the number of fully supported gain factors will be likely limited to two per each camera. The remaining gain factors will be available but unsupported so users of those modes will need to plan their

own calibration. The supported gain factors will provide the lowest readnoise and/or the better sampling of the detector full well. Further information about gain values for cycle 17 will be made available in the ACS Web page as soon as is available.

1.2.7 Flat Fields

WFC

The flat fields for the WFC combine information from two sources. Ground-based flats were obtained for all filters at a signal-to-noise of ~300 per pixel. To refine the low-frequency domain of the ground flats, inflight observations of a rich stellar field with large scale dithers have been analyzed (see ACS ISR 2002-08 and 2003-10). The required L-flat correction is a corner-to-corner gradient of 10 to 18%, dependent on wavelength. The resulting flat field supports photometry to ~1% over the full WFC field of view.

Figure 1.2 shows the corrected WFC ground flats for several broadband filters. **Note: the 50 pixel gap seen in external images, between the top and bottom chips, is not shown here**. Since the two CCDs were cut from the same Si wafer, and have undergone similar treatments, there is a significant continuity in the response across the gap.The central donut-like structure is wavelength dependent, where pixels in the central region are less sensitive than surrounding pixels in the blue F435W filter, for example, and more sensitive in the red F850LP filter. For further discussion of WFC flat fields, see ACS ISRs 2001-11, 2002-04, 2003-10, 2003-11, 2005-02, and 2005-09.

HRC

As for the WFC, the HRC ground flats were refined using in-flight observations of a rich stellar field with large scale dithers to determine the low-frequency domain of the flat fields. The correction required for the visible filters is a corner-to-corner gradient of 6% to 12%, dependent on wavelength. For the NUV filters, flats were taken in-flight using observations of the bright earth (see ACS ISR 2003-02) and include both the pixel-to-pixel and low-frequency structure of the detector response.

Currently, HRC flat fields have a signal-to-noise of ~300 per pixel and support photometry to ~1% over the full HRC field of view. Figure 1.3 shows the corrected HRC ground flats, derived for 6 broadband optical filters. The donut-like structure seen in the WFC response is not found in the HRC flats. For further discussion of HRC flat fields, see ACS ISRs 2001-11 and 2002-04.

Figure 1.2: WFC flat field.

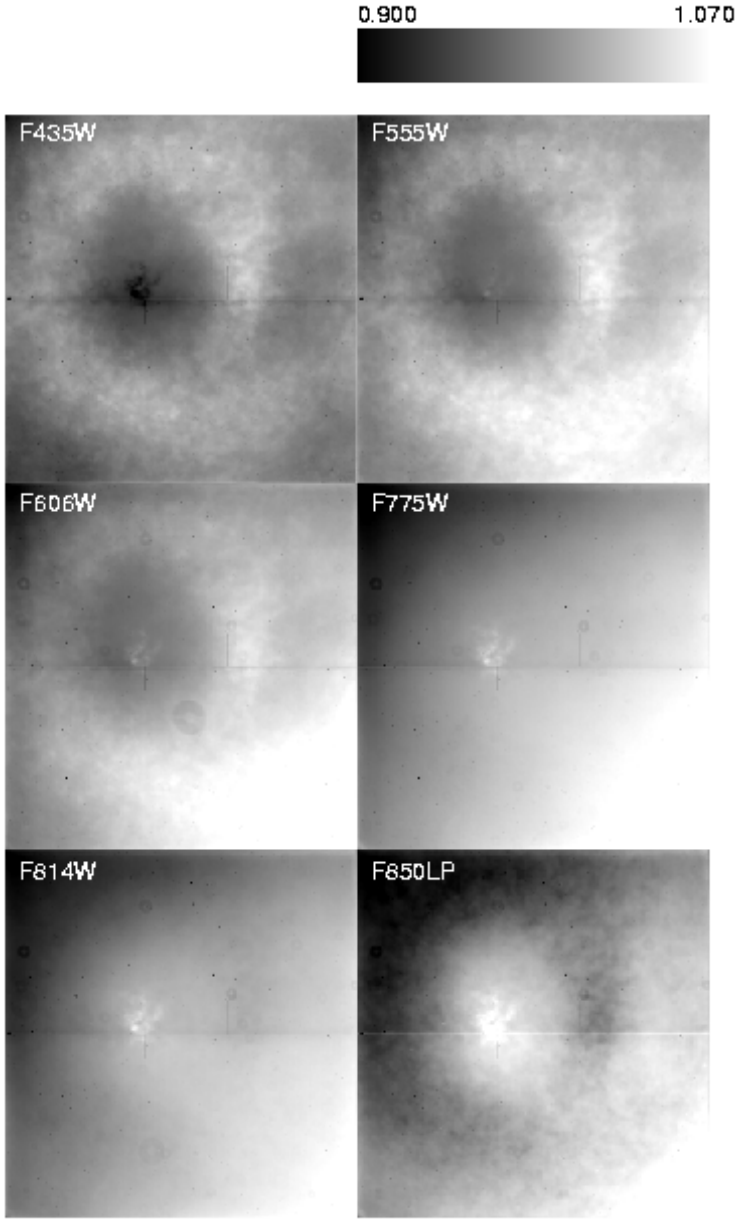

Figure 1.3: HRC flat field.

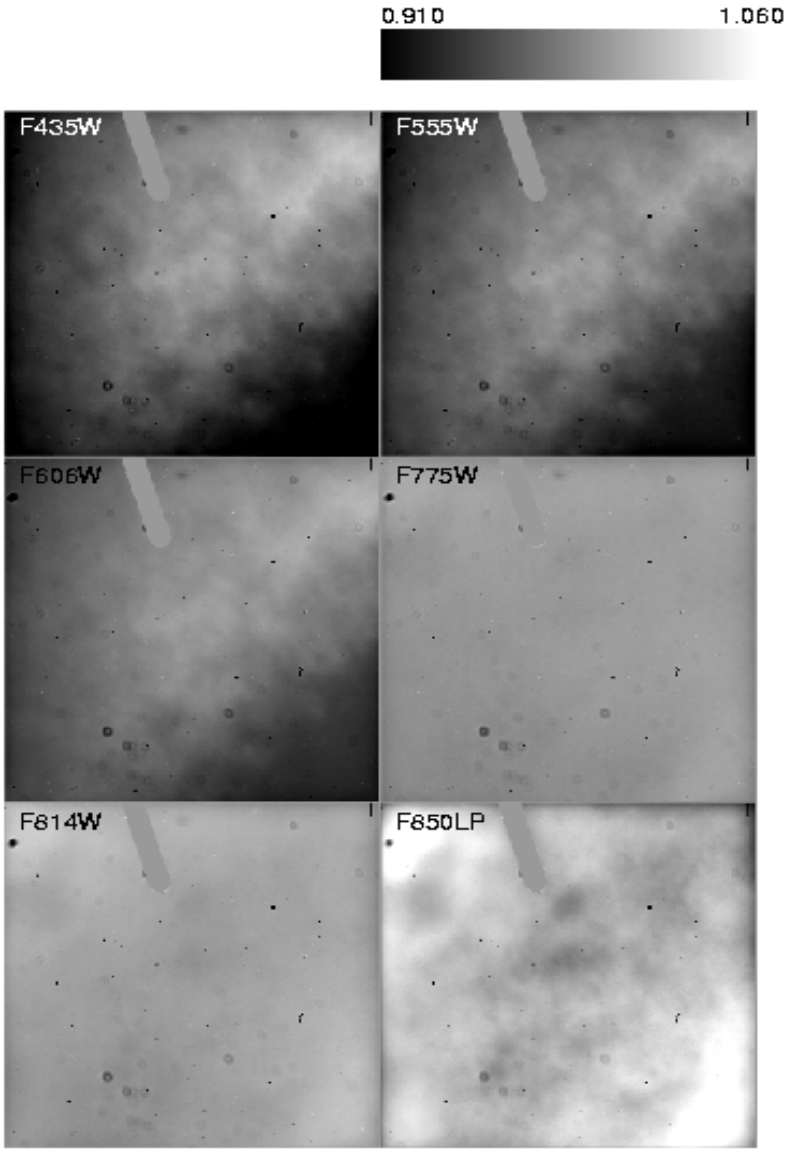

1.3 CCD Operations and Limitations

1.3.1 CCD Saturation: the CCD Full Well

The full well capacity for the ACS CCDs is given in Table 3.1 as 84,700 e^- for the WFC and 155,000 e^- for the HRC. This is somewhat dependent on the position on the chip, with variations of the order 10% and 18% across the field of view for the WFC and the HRC, respectively. If the CCD is over-exposed, blooming will occur. This happens when a pixel

becomes full, so excess charge flows into the next pixels along the column. However, extreme overexposure is not believed to cause any long-term damage to the CCDs, so there are no bright object limits for the ACS CCDs. When using GAIN=2 on the WFC and GAIN=4 on the HRC, it has been shown that the detector response remains linear to well under 1% up to the point when the central pixel reaches the full well depth. On-orbit tests have demonstrated that when using aperture photometry and summing over the surrounding pixels affected by bleeding, linearity to ≤ 1% holds even for cases in which the central pixel has received up to 10 times the full well depth (see ACS ISR 2004-01 for details). After the ACS repair, on-orbit tests will be devoted to characterize the linearity of both CCDs.

1.3.2 CCD Shutter Effects on Exposure Times

The ACS camera has a very high-speed shutter; even the shortest exposure times are not significantly affected by the finite traversal time of the shutter blades. On-orbit testing reported in ACS ISR 2003-03 has verified that shutter shading corrections are not necessary to support 1% photometry for either the HRC or WFC.

A total of 4 exposure times are known to be in error by up to 4.1%; the nominal 0.1 seconds HRC exposure is really 0.1041 seconds (updates for reference files have been made to use the correct values in pipeline processing). No significant differences exist between exposure times controlled by the two shutters (A and B), with the possible exception of non-repeatability up to ~1% on the WFC for exposures in the 0.7 to 2.0 second range. The HRC provides excellent shutter time repeatability.

1.3.3 Readnoise

WFC

We measured the readnoise level in the active area and overscan regions for all the amplifiers at the default gain settings. In general the readnoise has been constant with time. On June 29, 2003, just after a transit through the South Atlantic Anomaly (SAA) the readnoise in Amp A changed from ~4.9 to ~5.9 electrons rms. Although the telemetry did not show any anomaly in any component of the camera, it is likely that the readnoise jump was due to some sort of radiation damage. Amp A is the only amplifier that showed this anomaly. The amplitude of the variation (~1 e^-) was the same for GAIN 1 and 2. After the following anneal date the readnoise dropped to ~5.5 e^- and it remained constant for 27 days. After the following two anneal cycles the readnoise reached stability at ~5.6 e^- rms, approximately 0.7 e^- higher than before the change, and has remained constant since then. Figure 1.4 shows the readnoise in the image area for amplifier A during the “instability” period. The readnoise of all the other

amplifiers have been very stable since launch with post-launch figures almost unchanged from the pre-launch measurements made during ground testing.

Even with a slightly higher readnoise in Amp A most of the WFC broadband science observations are sky limited, while narrowband observations are primarily readnoise limited. Table 1.1 and Table 1.2 list the CCD gain measured under side-1 and side-2 operations. The ACS repair is expected to produce read noise levels comparable or better than listed for Side-1.

Figure 1.4: Readnoise jump in WFC Amp A (occurred on June 29, 2003).

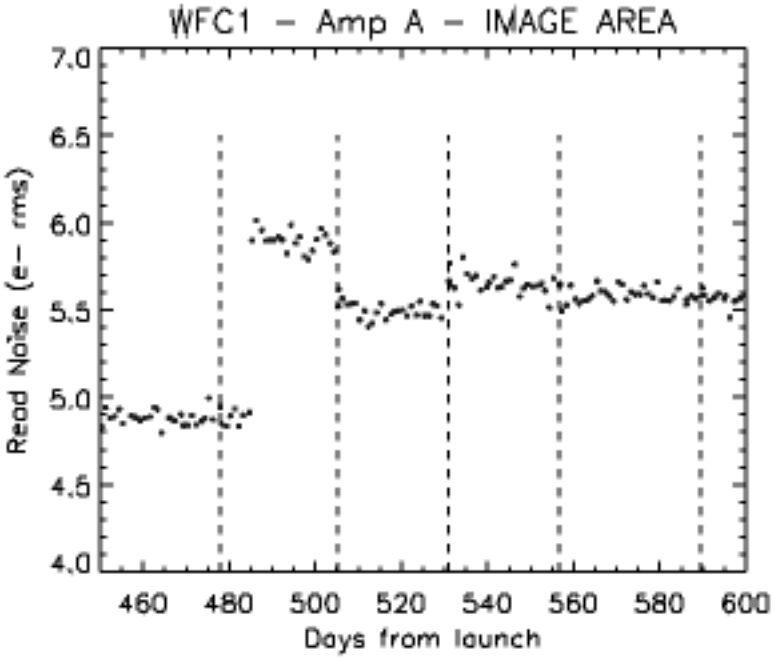

The vertical dashed lines indicate the annealing dates. See Table 1.1 for CCD gain and readout noise values.

HRC

The readnoise is monitored only for the default readout amplifier C at the default gain setting (2 e^-/DN). No variations have been observed with time. The readnoise measured in the image area (Tables 1.1 and 1.2) is in agreement with the readnoise measured in the two overscan regions, and it is comparable to the pre-flight value of 4.74 e^-.

1.3.4 Dark Current

All ACS CCDs are buried channel devices which have a shallow n-type layer implanted below the surface to store and transfer the collected signal charge away from the traps associated with the Si-SiO_2 interface.

Moreover, ACS CCDs are operated in Multi Pinned Phases (MPP) mode so that the silicon surface is inverted and the surface dark current is suppressed. ACS CCDs therefore have very low dark current. The WFC CCDs are operated in MPP mode only during integration, so the total dark current figure for WFC includes a small component of surface dark current accumulated during the readout time.

Like all CCDs operated in a low earth orbit radiation environment, the ACS CCDs are subject to radiation damage by energetic particles trapped in the radiation belts. Ionization damage and displacement damage are two types of damage caused by protons in silicon. The MPP mode is very effective in mitigating the damage due to ionization such as the generation of surface dark current due to the creation of trapping states in the Si-SiO_2 interface. Although only a minor fraction of the total energy is lost by a proton via nonionizing energy loss, the displacement damage can cause significant performance degradation in CCDs by decreasing the charge transfer efficiency (CTE), increasing the average dark current, and introducing pixels with very high dark current (hot pixels). Displacement damage to the silicon lattice occurs mostly due to the interaction between low energy protons and silicon atoms. The generation of phosphorous-vacancy centers introduces an extra level of energy between the conduction band and the valence band of the silicon. New energetic levels in the silicon bandgap have the direct effect of increasing the dark current as a result of carrier generation in the bulk depletion region of the pixel. As a consequence, the dark current of CCDs operated in a radiative environment is predicted to increase with time.

Ground testing of the WFC CCDs, radiated with a cumulative fluence equivalent to 2.5 and 5 years of on-orbit exposure, predicted a linear growth of ~1.5 e^-/pixel/hour/year.

The dark current in ACS CCDs is monitored four days per week with the acquisition of four 1000 seconds dark frames (totaling 16 images per week). Dark frames are used to create reference files for the calibration of scientific images, and to track and catalog hot pixels as they evolve. The four daily frames are combined together to remove cosmic rays and to extract hot pixel information for any specific day. The dark reference files are generated by combining two weeks of daily darks in order to reduce the statistical noise. The hot pixel information for a specific day is then added to the combined bi-weekly dark. In order to study the evolution of the dark current with time, the modal dark current value in the cosmic-ray free daily darks is calculated. As expected, the dark current increases with time (Figure 1.5). The observed linear growth rates of dark current are 2.1 and 1.6 e^-/pixel/hour/year for WFC1 and WFC2 respectively, and 2.1 e^-/pixel/hour/year for the HRC CCD. These rates are in general agreement with the ground test predictions.

Simultaneously to the beginning of the side-2 operation in July 2006 the temperature set point of the WFC has been lowered from -77 C to -80 C (see ACS TIR 2006-02).

Dark current and hot pixels depended strongly on the operating temperature. The reduction of the operating temperature of the WFC CCDs reduced them by almost 50%. The dark rate shows a clear drop on July 4, 2006, when the temperature was changed, and Figures 4.7 and 4.8 illustrate the before-and-after effect directly. The new operating temperature brought the dark current of the WFC CCDs back to the level eighteen months after the launch.

Figure 1.5: Dark rate trend with time for the WFC CCDs.

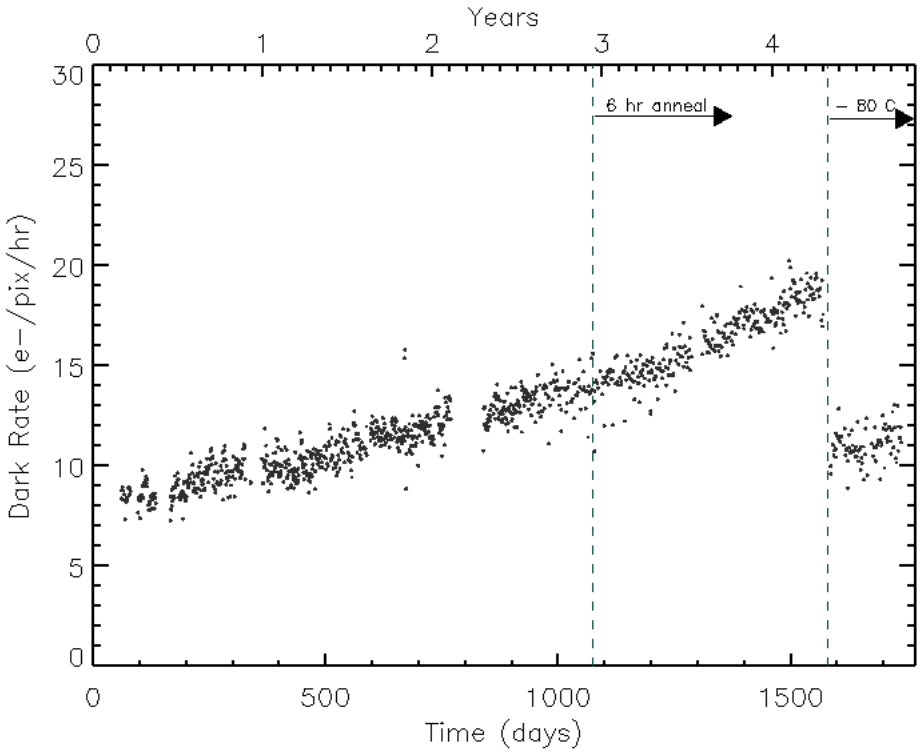

Dark current as a function of time for one of the WFC CCDs. The first dashed line indicates the change in the anneal procedure from twelve to six hours for the duration of the warm-up period. The shorter anneal slightly increased the rate of growth of the dark current. The second dashed line indicates the change in temperature set point for the CCDs. As expected the dark current dropped drastically at the new temperature.

Figure 1.6: Dark current as a function of time for the HRC

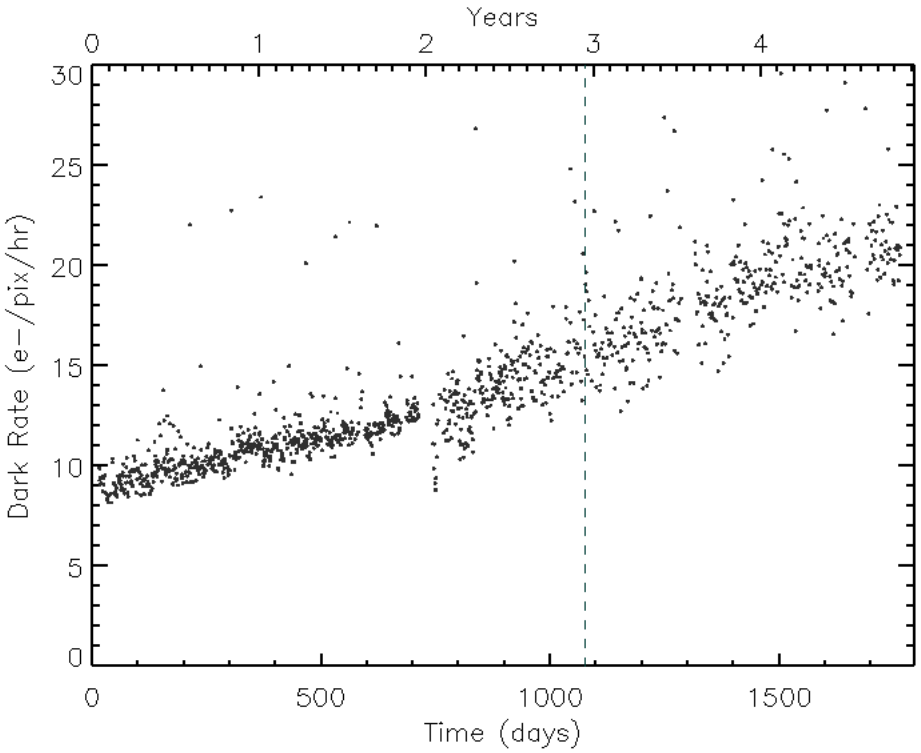

Figure 1.7: Histogram of WFC dark frames taken before and after the change in temperature.

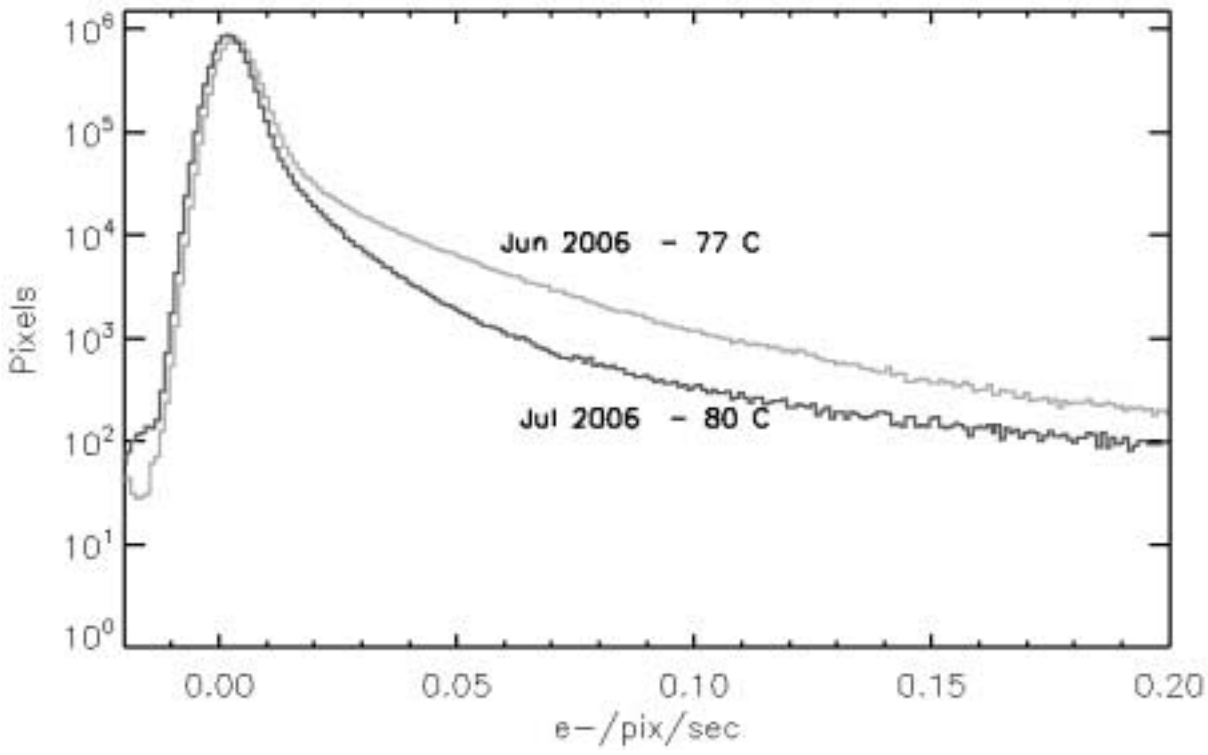

Figure 1.8: Sub-section of WFC dark frames showing hot pixel contamination before and after the change in temperature on July 4, 2006

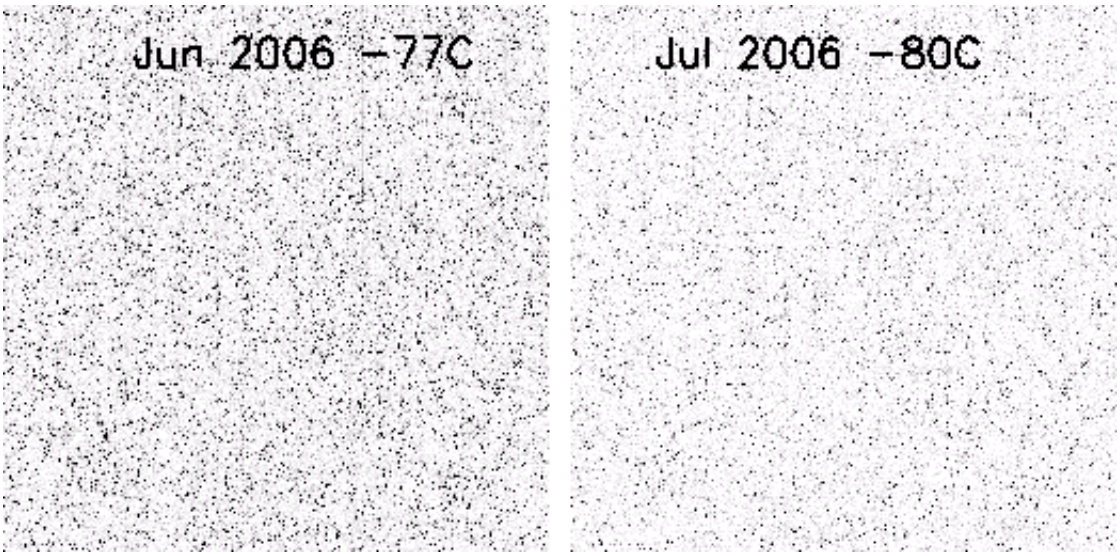

1.3.5 Warm and hot pixels

In the presence of a high electric field, the dark current of a single pixel can be greatly enhanced. Such pixels are called dark spikes or hot pixels. Although the increase in the mean dark current with proton irradiation is important, of greater consequence is the large increase in dark current nonuniformity.

We have chosen to classify the field-enhanced dark spikes into two categories: warm and hot pixels. The definition of “warm” and “hot” pixel is somewhat arbitrary. We have chosen a limit of 0.08 e^-/pixel/seconds as a threshold above which we consider a pixel to be “hot”. We identify “warm” pixels as those which exceed by about 5 σ (~0.02 e^-/pixel/second) the normal distribution of the pixels in a dark frame up to the threshold of the hot pixels (See Figure 1.11) for a typical dark rate pixel distribution)

Warm and hot pixels accumulate as a function of time on orbit. Defects responsible for elevated dark rate are created continuously as a result of the ongoing displacement damage on orbit. The number of new pixels with a dark current higher than the mean dark date increases every day by few to several hundreds depending on the threshold. The reduction of the operating temperature of the WFC CCDs has dramatically reduced the dark current of the hot pixels and therefore many pixels previously classified as hot are now warm or normal pixels.

Table 1.3: Creation rate of new hot pixels (pixel/day).

Threshold (e^-/pixel/second)	WFC(-77 C)	WFC (-80 C)	HRC(-81 C)
0.02	815 56	N.A.	125 12
0.04	616 22	427 34	96 2
0.06	480 13	292 8	66 1
0.08	390 9	188 5	48 1
0.10	328 8	143 12	35 1
1.00	16 1	10 1	1 0.5

Table 1.4: Annual permanent hot pixel contamination (%).

Threshold (e^-/pixel/second)	WFC(-77 C)	WFC (-80 C)	HRC(-81 C)
>0.02	1.60	N.A.	1.54
>0.04	0.78	0.32	0.52
>0.06	0.46	0.18	0.29
>0.08	0.30	0.16	0.21
>0.10	0.23	0.13	0.17
>1.0	0.03	0.02	0.02

Most of these new hot pixels are transient. Like others CCDs on HST, the ACS devices undergo a monthly annealing process. The CCDs and the thermal electric coolers (TECs) are turned off and the heaters are turned on to warm the chips to ~19 °C. Although the annealing mechanism at such low temperatures is not yet understood, after this “thermal cycle” the population of hot pixels is greatly reduced (see Figure 1.9). The anneal rate depends on the dark current rate with very hot pixels being annealed easier than warmer pixels. For pixels classified as “hot” (those with dark rate > 0.08 e^-/pix/sec) the anneal rate is ~82% for WFC and ~86% for HRC.

Annealing has no effect on the normal pixels that are responsible for the increase in the mean dark current rate. Such behavior is similar to what is seen with STIS SITe CCD and WFC3 CCDs during ground radiation testing.

Figure 1.9: Hot pixel growth in the WFC CCDs.

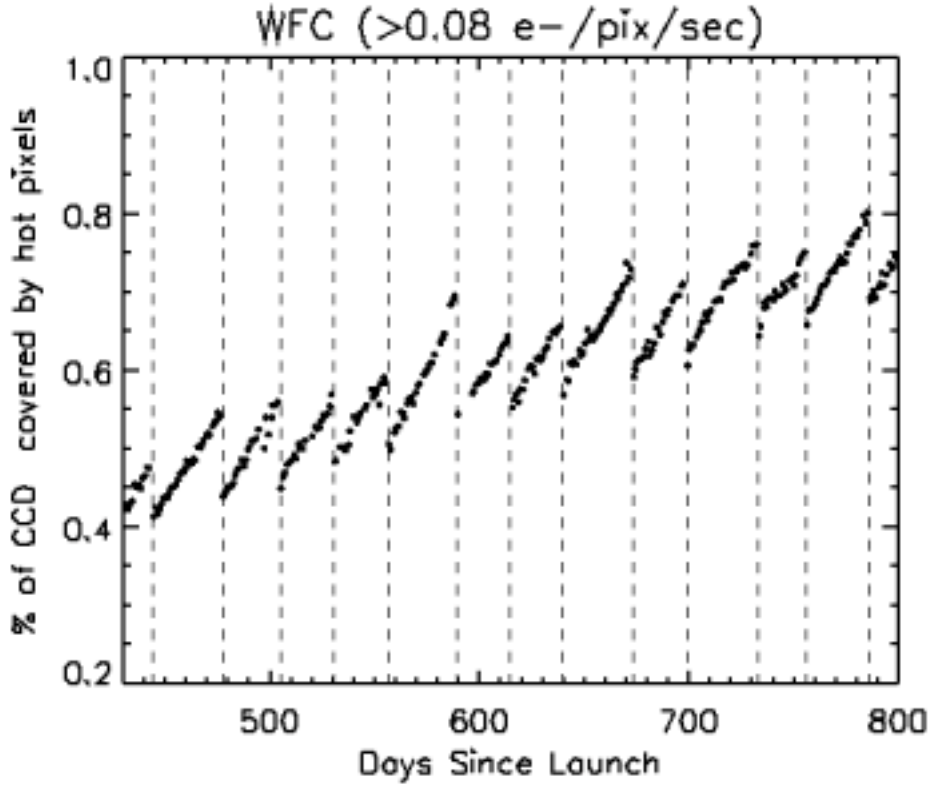

The vertical dashed lines indicate the annealing dates.

During early annealing episodes the ACS CCDs were warmed up for 24 hours. But the annealing time was reduced to 6 hours in spring of 2004 to allow better scheduling of HST time. Even with a shorter cycle the effectiveness of the anneal in ACS CCDs has remained the same. It is interesting to note that since ACS launch, four HST safing events have occurred; after each event the population of hot pixels was reduced as if a normal anneal cycle has occurred. During the safing events the CCDs and the TECs were turned off. Since the heaters were not turned on, the CCDs warmed-up to only about −10 °C. After a period of time ranging from 24 to 48 hours, HST resumed normal operation. The dark frames taken after the safing events showed a reduction in hot pixel population similar to those observed during normal annealing cycles.

Since the anneals cycle do not repair 100% of the hot pixels, there is a growing population of permanent hot pixels (see Figure 1.10 and Figure 1.11).

Figure 1.10: A subsection of WFC1 dark frames taken at different epochs showing the increasing population of hot pixels.

From left to right: before launch, and after 1, 2 and 3 years on orbit.

Figure 1.11: Histogram of WFC dark frames taken at different epochs.

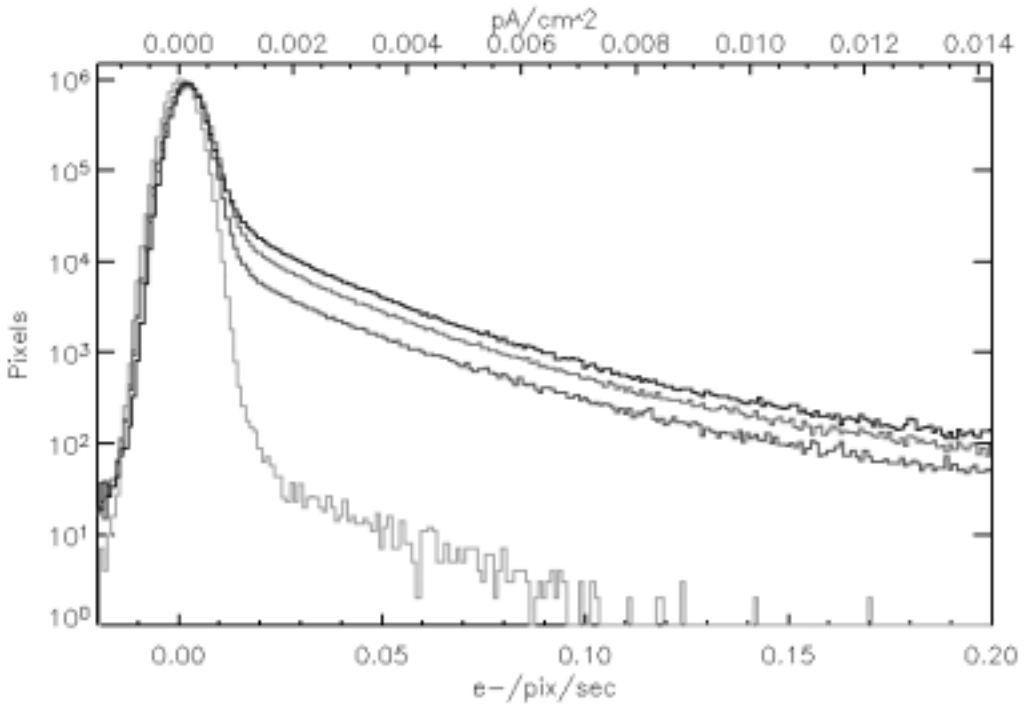

Epochs pre-launch, and after 1,2, and 3 years on orbit. Both the mean dark rate increase and the growing population of permanent hot pixels are visible.

According to the current trend, about 0.3% of WFC (0.22% of HRC) pixels became permanently hot every year (see Table 1.5). In a typical 1000 second exposure the percentage of pixels contaminated by cosmic rays ranges between 1.5% and 3% of the total. By spring of 2007 the contamination from hot pixels will impact about 2% of the pixels (See Figure 1.12.).

Table 1.5: Permanent warm and hot pixel growth (%/yr).

Threshold (e^-/pix/sec)	WFC	HRC
0.02	174	1.52
0.04	0.86	0.50
0.06	0.50	0.31
0.08	0.30	0.22
0.10	0.25	0.18
1.00	0.04	0.03

In principle, warm and hot pixels could be eliminated by the superdark subtraction. However, some pixels show a dark current that is not stable with time but switches between well defined levels. These fluctuations may have timescales of a few minutes and have the characteristics of random telegraph signal (RTS) noise. The dark current in field-enhanced hot pixels can be dependent on the signal level, so the noise is much higher than the normal shot noise. As a consequence, since the locations of warm and hot pixels are known from dark frames, they are flagged in the data quality. The hot pixels can be discarded during image combination if multiple exposures have been dithered.

While the standard CR-SPLIT approach allows for cosmic ray subtraction, without additional dithering, it will not eliminate hot pixels in post-observation processing.

We recommend that observers who would have otherwise used a simple CR-SPLIT now use some form of dithering instead. Any form of dithering providing a displacement of at least a few pixels can be used to simultaneously remove the effects of cosmic ray hits and hot pixels in post-observation processing.

For example, a simple `ACS-WFC-DITHER-LINE` pattern has been developed, based on integer pixel offsets, which shifts the image by 2 pixels in X and 2 pixels in Y along the direction that minimizes the effects of scale variation across the detector. The specific parameter values for this pattern are given on the ACS dithering Web page at:

`http://www.stsci.edu/hst/acs/proposing/dither.`

Additional information can be found in the *Phase II Proposal Instructions*.

Given the transient nature of hot pixels, users are reminded that a few hot pixels may not be properly flagged in the data quality array (because

they spontaneously “healed” or because their status changed in the period spanning the reference file and science frame acquisition), and therefore could create false positive detections in some science programs.

Figure 1.12: Growth of permanent warm and hot pixel population as a function of time (WFC top, HRC bottom).

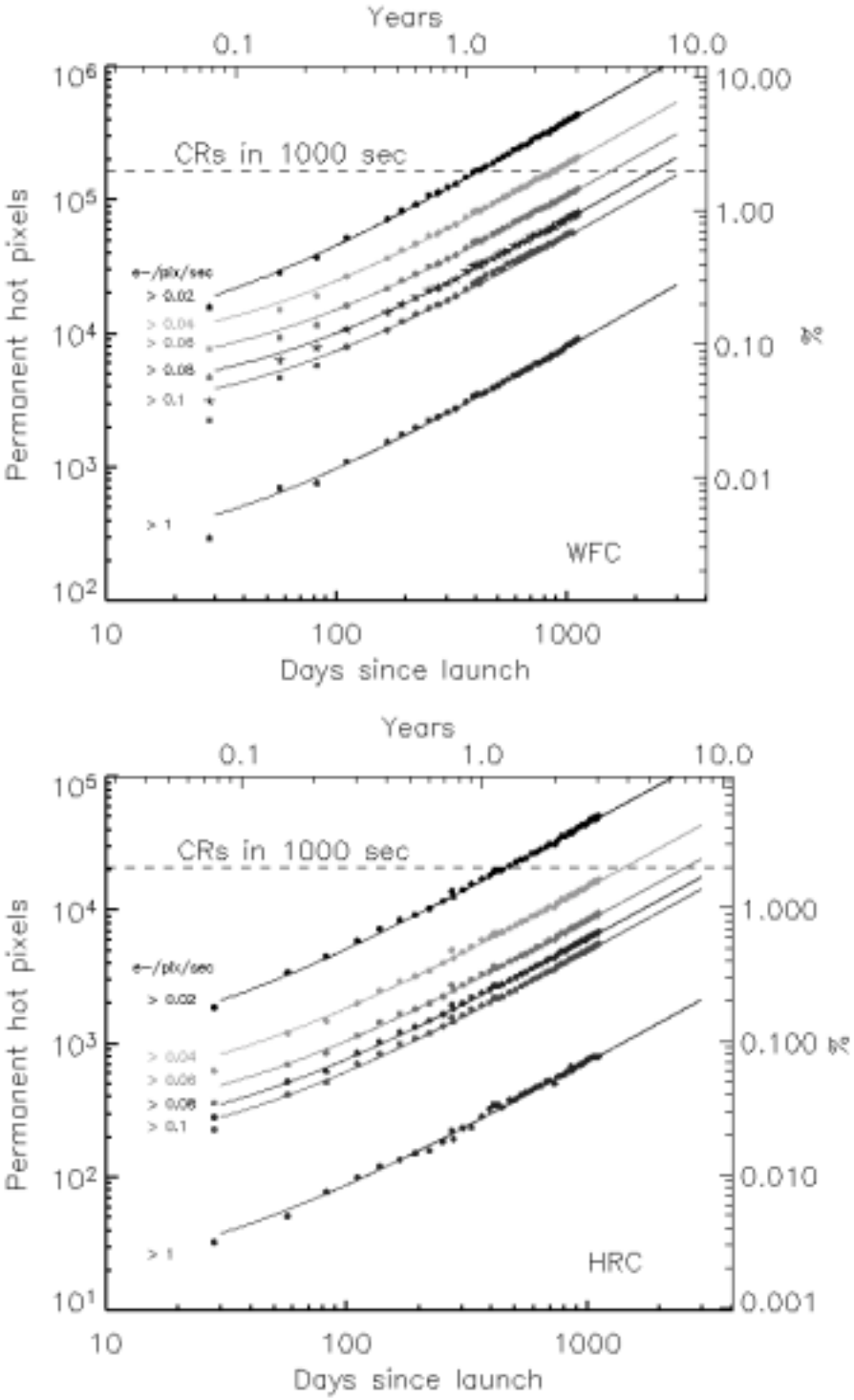

The contamination level due to cosmic rays accumulated in a 1000 second exposure is shown with a dashed line.

1.3.6 Cosmic Rays

Initial studies have been made of the characteristics of cosmic ray impacts on the HRC and WFC. The fraction of pixels affected by cosmic rays varies from 1.5% to 3% during a 1000 second exposure for both cameras, similar to what was seen on WFPC2 and STIS. This number provides the basis for assessing the risk that the target(s) in any set of exposures will be compromised. The affected fraction is the same for the WFC and HRC despite their factor of two difference in pixel areas because the census of affected pixels is dominated by charge diffusion, not direct impacts. Observers seeking rare or serendipitous objects, as well as transients, may require that every single WFC pixel in at least one exposure among a set of exposures is free from cosmic ray impacts. For the cosmic ray fractions of 1.5% to 3% in 1000 seconds, a single ~2400 second orbit must be broken into 4 exposures of 500 to 600 seconds each to reduce the number of uncleanable pixels to 1 or less. Users seeking higher S/N (lower readnoise) may prefer the trade-off of doing 3 exposures of ~800 seconds, where CR-rejection should still be very good for most purposes. But we do NOT recommend 2 long exposures (1.e. 1200 seconds), where residual CR contamination would be unacceptably high in most cases. We recommend that users dither these exposures to remove hot pixels as well as cosmic rays (see Section 7.4).

The flux deposited on the CCD from an individual cosmic ray does not depend on the energy of the cosmic ray but rather the length it travels in the silicon substrate. The electron deposition due to individual cosmic rays has a well defined cut-off with negligible events of less than 500 e^- and a median of ~1000 e^- (see Figure 1.13 and Figure 1.14).

Figure 1.13: Electron deposition by cosmic rays on WFC.

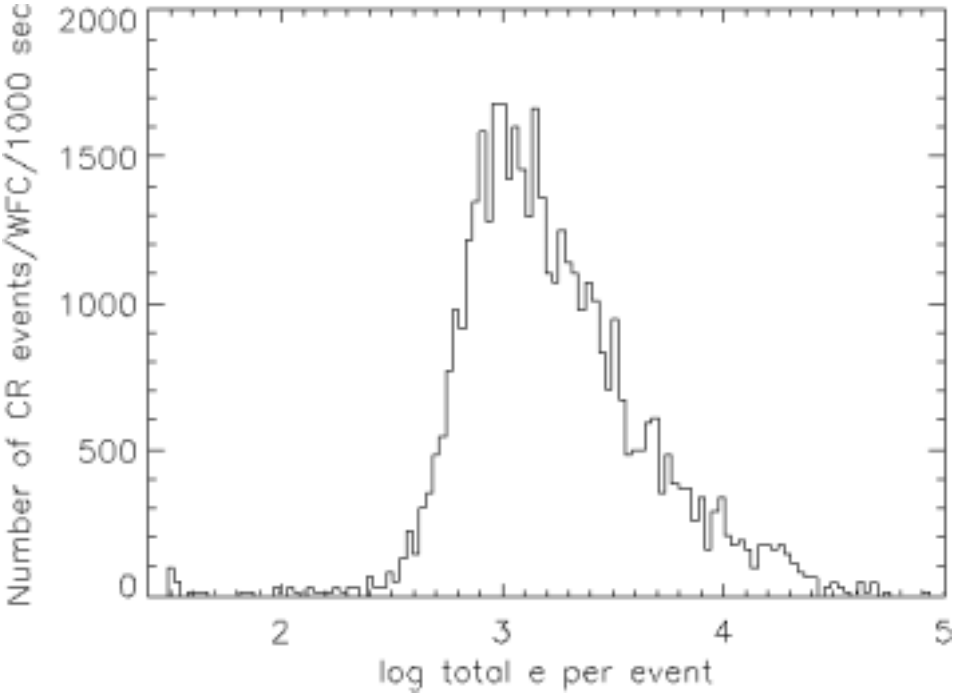

Figure 1.14: Electron deposition of cosmic rays on HRC.

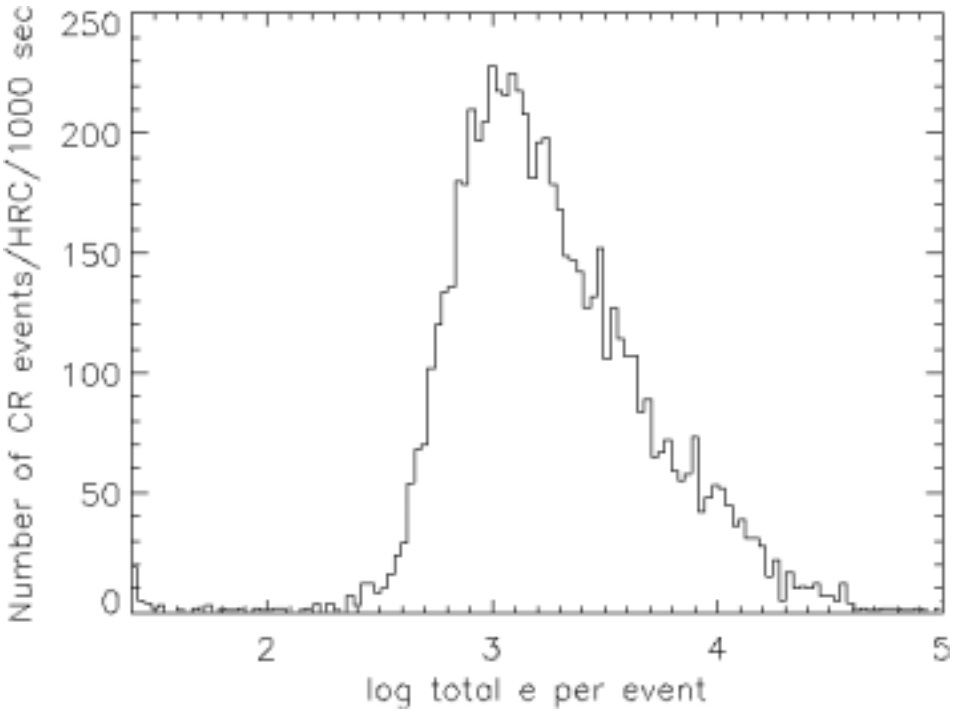

The distribution of the number of pixels affected by a single cosmic ray is strongly peaked at 4 to 5 pixels. Although a few events are seen which encompass only one pixel, examination of these events indicate that at least

some, and maybe all of these sources are actually transient hot pixels or unstable pixels which can appear hot in one exposure (with no charge diffusion) and normal in the next. Such pixels are very rare but do exist. There is a long tail in the direction towards increasing numbers of attached pixels.

Distributions of sizes and anisotropies can be useful for distinguishing cosmic rays from astrophysical sources in a single image. The size distribution for both chips peaks near 0.4 pixels as a standard deviation (or 0.9 pixels as a FWHM). This is much narrower than for a PSF and is thus a useful discriminant between unresolved sources and cosmic rays.

1.3.7 Charge Transfer Efficiency

Charge transfer efficiency (CTE) is a measure of how effective the CCD is at moving charge from one pixel location to the next when reading out the chip. A perfect CCD would be able to transfer 100% of the charge as the charge is shunted across the chip and out through the serial register. In practice, small traps in the silicon lattice compromise this process by holding on to electrons, releasing them at a later time. (Depending on the trap type, the release time ranges from a few microseconds to several seconds). For large charge packets (several thousands of electrons), losing a few electrons along the way is not a serious problem, but for smaller (~100 e^- or less) signals, it can have a substantial effect.

CTE is typically measured as a pixel transfer efficiency, and would be unity for a perfect CCD. The CTE numbers for the ACS CCDs at the time of installation are given in Table 1.6. While the numbers look impressive, remember that reading out the WFC CCD requires 2048 parallel and 2048 serial transfers, so that almost 2% of the charge from a pixel in the corner opposite the readout amplifier is lost.

Table 1.6: Charge transfer efficiency measurements for the ACS CCDs at installation time (Fe55 test at 1620 e^-).

Chip	Parallel	Serial
WFC1	0.999995	0.999999
WFC2	0.999995	0.999999
HRC	0.999983	0.999994

Also, the CTE numbers are significantly different for images where the pixels have a low intensity compared to those where the intensity is high.

Both the WFPC2 and STIS CCDs have been found to suffer from a significant degradation in CTE since their installation in 1993 and 1997, respectively. At the end of Cycle 11 we performed the first on-orbit calibration of the photometric losses due to imperfect CTE on ACS HRC

and WFC and monitored CTE effects on photometry during the following cycles (11-14). We used images of 47 Tucanae to measure the dependence of stellar photometry on the number of parallel and serial transfers. The results are described by Riess et al. (ACS ISR 2003-09) and are summarized here. For WFC, significant photometric losses are apparent for stars undergoing numerous parallel transfers (y-direction). Extrapolated to 2008, the losses should be 3% for typical observing parameters, rising to ~15% in worst cases (faint stars, low background). The size of the photometric loss appears to have a strong power-law dependence on the stellar flux, as seen for other CCDs flown on HST.

The dependence on background is significant but for faint targets there is little advantage to increasing the background intentionally (e.g., by post-flashing) due to the added shot noise. However, in some specific cases, it may instead be useful to choose the filter in order to obtain a higher background (e.g. F606W). CTE degradation has also an impact on astrometry (see ACS ISR 2007-04). Therefore, for astrometric programs of relatively bright objects, the use of post-flash may be considered. No losses are apparent for WFC due to serial transfers (x-direction). For HRC, significant photometric losses also arise from parallel transfer (extrapolating to 2008, ~3% for typical observations, ~20% for worst case) but are not seen for serial transfer. Correction formulae are presented in ACS ISR 2004-06 to correct photometric losses as a function of a source's position, flux, background, time, and aperture size. Updated formulae are in course of development and will substitute the previous ones. Users are encouraged to check the ACS Web page for updates.

Figure 1.15 shows the predicted photometric losses for the WFC due to imperfect parallel CTE as a function of time. These curves are based on the formulae published in ACS ISR 2004-06 and require extreme extrapolation, therefore they should be used for planning purposes only. Four specific science applications are shown as examples: the measurement of the faint end of M31's CMD (GO 9453), the measurement of high-redshift supernovae (GO 9528), the measurement of any PSF whose brightness is the zeropoint (i.e., 1 e^-/second), and photometry of a 20^{th} magnitude star in a narrow band.

Figure 1.15: Projected CTE losses in WFC (and equivalently, the size of corrections).

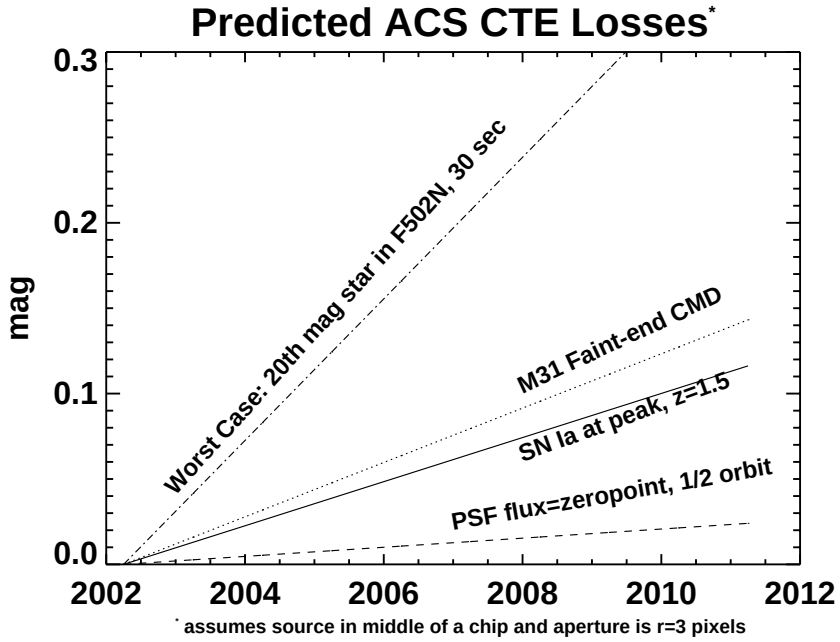

Projected CTE losses in WFC for sample science applications described in Table 1.7. The precision of measurements is not limited by the size of the loss but rather its uncertainty. As a rule of thumb we suggest that the ultimate limit of precision will be ~25% of the loss after correction.

Table 1.7: Example of science applications and their assumed parameters.

Science application	Source flux (e^-)	Sky (e^-)
SN Ia at peak z = 1.5	100	30
M31 faint-end of CMD	40	100
PSF e^-/sec, 1/2 orbit	1000	40
F502N, 30 sec, 20^{th} mag star	258	0.1

When observing a single target significantly smaller than a single detector, it is possible to place it near an amplifier to reduce the impact of imperfect CTE. This is easy to accomplish by judicious choice of aperture and target position, or by utilizing POS TARG commands. However, be aware that large POS TARGs are not advisable because they change the fractional pixel shifts of dither patterns due to the geometric distortion of ACS. An alternative means to achieve the placement of a target near the amplifier is by using some of the subarray apertures. For example, `WFC1-512` (target will have 256 transfers in X and Y), `WFC1-1K`, and `WFC1-2K` place the target near the B amplifier (or `WFC2-2K` for the C amplifier).

1.3.8 UV Light and the HRC CCD

In the optical, each photon generates a single electron. However, in the near-UV, shortward of ~3200 Å there is a finite probability of creating more than one electron per UV photon (see Christensen, O., *J. App. Phys.* **47**,689, 1976). At room temperature the theoretical quantum yield (i.e., the number of electrons generated for a photon of energy $E > 3.5eV$ (λ~3500 Å)), is $Ne = E(eV)/3.65$. The HRC CCDs quantum efficiency curve has not been corrected for this effect. The interested reader may wish to see the *STIS Instrument Handbook* for details on the signal-to-noise treatment for the STIS CCDs.

1.4 The SBC MAMA

1.4.1 MAMA Properties

The ACS MAMA detector is the STIS flight spare STF7. It provides coverage from 1150 Å to 1700 Å. The MAMA detector is a photon-counting device which processes events serially. The ACS MAMA only operates in the accumulate (ACCUM) mode, in which a time-integrated image is produced. Unlike the STIS MAMAs, the ACS does not offer the high-resolution (2048×2048) mode or time-tagged data acquisition. The primary benefits afforded by the STIS and ACS MAMAs, in comparison with previous HST UV spectroscopic detectors such as those in the GHRS and FOS, are high spatial resolution, two-dimensional imaging over a relatively large field of view, and low background for point sources.

Figure 1.16: Design of the SBC MAMA.

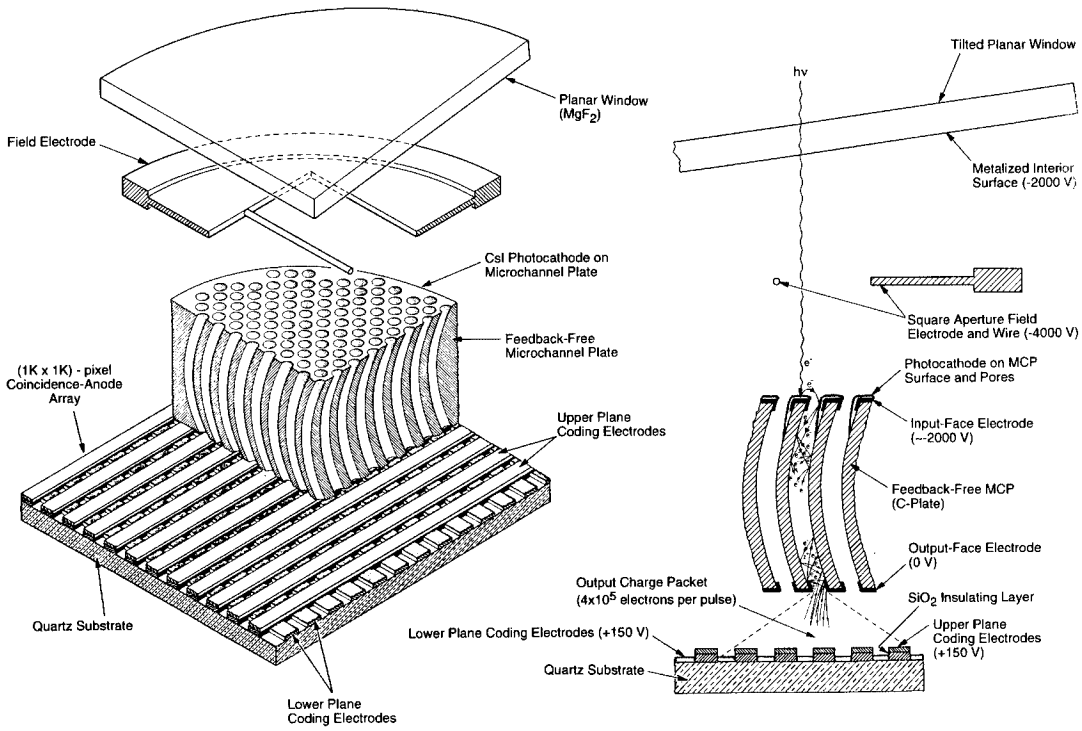

Figure 1.16 illustrates the design of the MAMA, which has an opaque CsI photocathode deposited directly on the face of the curved microchannel plate (MCP). Target photons strike the photocathode, liberating single photoelectrons which pass into the MCP. There they are multiplied to a pulse of ~4×10^5 e^-. The pulse is recorded by an anode array behind the photocathode, and detected by the MAMA electronics which rejects false pulses and determines the origin of the photon event on the detector.

The field electrode, or *repeller wire*, repels electrons emitted away from the microchannel plate back into the channels. This provides an increase in quantum efficiency of the detector at the price of an increase in the detector point spread function halo. The repeller wire voltage is always on for SBC observations.

Table 1.8: SBC detector performance characteristics.

Characteristic	SBC MAMA performance
Photocathode	CsI
Wavelength range	~1150 to1700 Å
Pixel format	1024×1024 pixel
Pixel size	25×25 μm
Plate scale	$\sim 0.034 \times 0.030$ ″/pixel
Field of view	34.6″ x 30.8″
Quantum efficiency	19.2% @ 1216 Å
Dark count[1]	$\sim 5 \times 10^{-5}$ e^-/second/pixel
Global count-rate linearity limit[2]	360,000 counts/second
Local count-rate linearity limit	~350 counts/second/pixel
Visible light DQE	$< 1.2 \times 10^{-9}$ above 400 nm

1. The dark count increases with the length of time the SBC is turned on, beginning at about 10^{-5} electrons/pixel/second and increasing by about a factor of five over two hours.
2. Rate at which counting shows 10% deviation from linearity. These count rates are well above the bright-object screening limits.

1.4.2 SBC Spectral Response

The total transmission curve for the SBC with the PR110L prism is shown in Figure 1.17. The peak photocathode response occurs at Lyman-α. Its spectral response is defined by the cutoff of the MgF_2 window at 1150 Å at short wavelengths, and by the relatively steep decline of the CsI photocathode at long wavelengths.

Recent observations of flux calibration stars and a G-type star using the SBC PR110L prism have revealed that the sensitivity of the MAMA detector to optical and near-UV light is apparently much larger than previously thought.

Preliminary estimates of the real SBC throughput indicates that the detector efficiency is factors of approximately 50 and 1000 higher at wavelengths of 3000 and 4000 Å respectively compared to ground testing. For a solar type spectrum, this can mean that one-half or more of the counts detected are due to optical and near-UV photons, rather than from the expected FUV photons. There is also some evidence that this red leak changes as the SBC detector warms up, increasing by as much as 30% over the course of 5 orbits. It is not yet clear if this red leak has also been

increasing secularly over time. STIS FUV MAMA data seem to show a similar, although perhaps somewhat smaller effect.

For dispersed PR110L and PR130L observations, it is straightforward to identify this extra red light; however, it clearly also affects SBC imaging observations done with the long pass filters. Until this effect is better understood and calibrated, extreme caution should be used when interpreting FUV imaging observations of red targets. Observers who need to measure FUV fluxes of red targets may wish to consider interleaving observations with two different SBC long pass filters (e.g., F140LP and F165LP), so that the difference in the count rates can be used to isolate the true FUV flux.

Figure 1.17: Total transmission curve for ACS SBC plus the PR110L prism

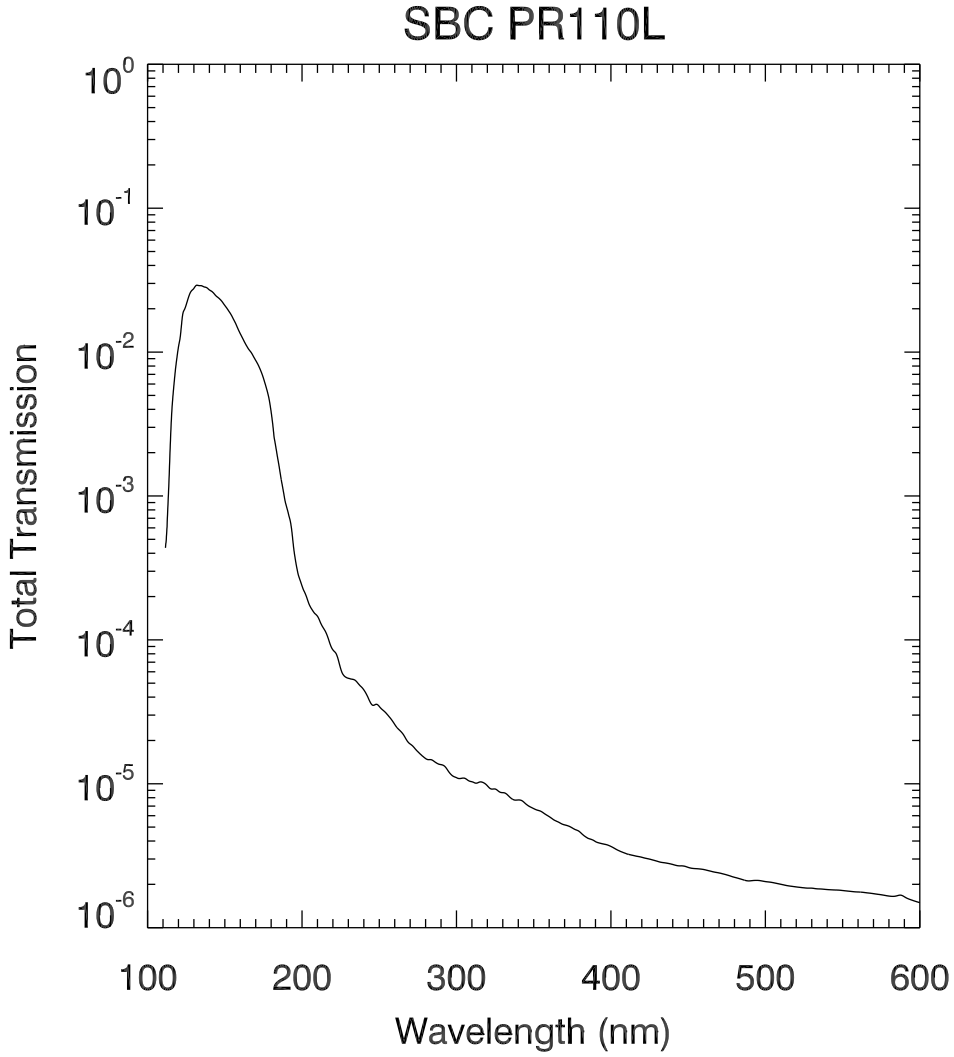

1.4.3 Optical Performance

The SBC exhibits low-level extended wings in the detector point-spread function (PSF). Sample MAMA detector PSF profiles are shown in Figure 1.18.

Figure 1.18: MAMA point spread function.

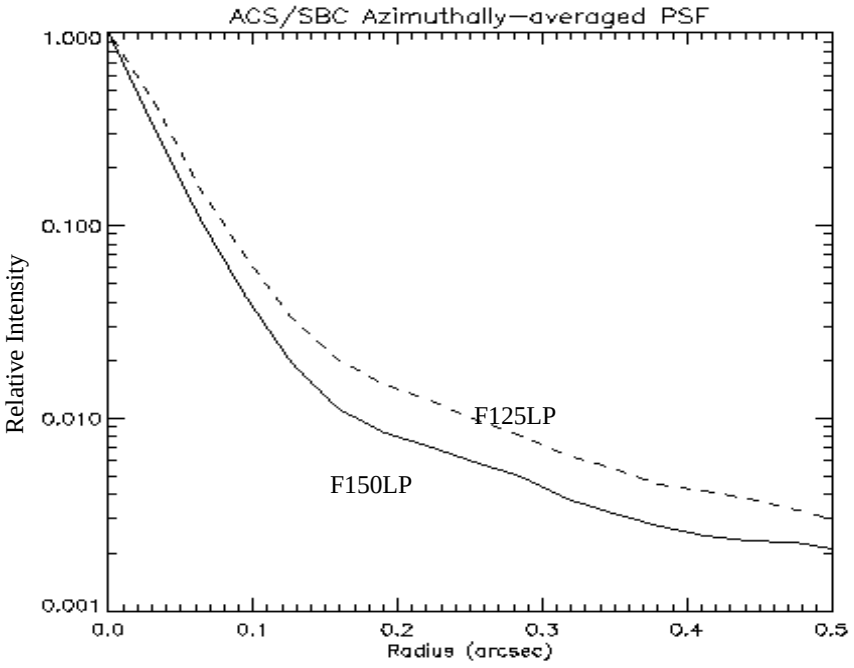

1.5 SBC Operations and Limitations

1.5.1 SBC Scheduling Policies

The STIS MAMA control electronics are subject to resets due to cosmic-ray upsets. Therefore, STIS MAMAs were operated only during the contiguous orbits of each day that are free of the South Atlantic Anomaly (SAA). Even though the design of the ACS MAMA control electronics in the SBC was modified so that they would not be susceptible to cosmic-ray hits, the background count rate still exceeds the bright object limits for the SBC during SAA passage. Consequently, the SBC will in general only be scheduled for use during SAA-free orbits.

1.5.2 MAMA Overflow of the 16 Bit Buffer

The MAMA is a photon-counting detector: as each event is recorded, the buffer memory for the corresponding pixel is incremented by one integer. The buffer memory stores values as 16 bit integers; hence the maximum number it can accommodate is 65,535 counts per pixel in a given ACCUM mode observation. The 2-Byte (16-bit) memory can hold 2^{16} values, including 0. When accumulated counts per pixel exceed this number, the values will wrap, i.e. the memory resets to 0. As an example, if you are counting at 25 counts/second/pixel, you will reach the MAMA "accumulation" limit in ~44 minutes.

One can keep accumulated counts per pixel below this value by breaking individual exposures into multiple identical exposures, each of which is short enough that fewer than 65,535 counts are accumulated per pixel. There is no readnoise for MAMA observations, so no penalty is paid in lost signal-to-noise ratio when exposures are split. There is only a small overhead for each MAMA exposure (see Section 8.2).

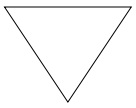

Keep the accumulated counts per SBC pixel below 65,535 by breaking single exposures into multiple exposures, as needed.

1.5.3 MAMA Darks

MAMA detectors have intrinsically low dark currents. Ground test measurements of the ACS MAMA showed count rates in the range of 10^{-5} to 10^{-4} counts per pixel per second as the temperature varied from 28 °C to 35 °C degrees. The count rate increased by about 30% for one degree increase in temperature. In-flight measurements, taken weekly throughout June and July 2002, show count rates between $8x10^{-6}$ and 10^{-5}. These measurements were taken as soon as the MAMA was turned on and were therefore at the lower end of the temperature range. A 10 hour observation in SMOV, long enough for nominal temperatures to be reached, yielded a dark current of 1.2×10^{-5} counts per second per pixel. Monthly monitoring shows the in-flight dark current to be about $9x10^{-6}$ counts per second per pixel. For typical SBC operations in which the detector is turned on for less than two hours, a dark image collected at lower temperatures is more suitable and replaces the current calibration image. This has a mean dark rate of 10^{-5} counts per second per pixel.

Recent measurements of SBC darks have shown a significant increase in the rate when the detector is on for several hours. The rate for the first two years remains close to 10^{-5} counts per second per pixel but after 5 hours the rate is 5×10^{-5} counts per second per pixel. When last measured in 2002 this time dependant effect was almost negligible.

The ACS MAMA has a broken anode which disables rows 599 to 605. There are three dark spots smaller than 50 microns at positions (334,977), (578,964), and (960,851), as well as two bright spots at (55,281) and (645,102) with fluctuating rates that are always less than 3 counts per second. The reference pixel has been moved to (512,400) to avoid these areas (see Table 7.10)

An example of the dark current variation across the detector can be seen in Figure 1.19 below.

Figure 1.19: MAMA dark image. Full frame MAMA dark image. The average dark rate in this image is 5×10^{-5} counts per second per pixel.

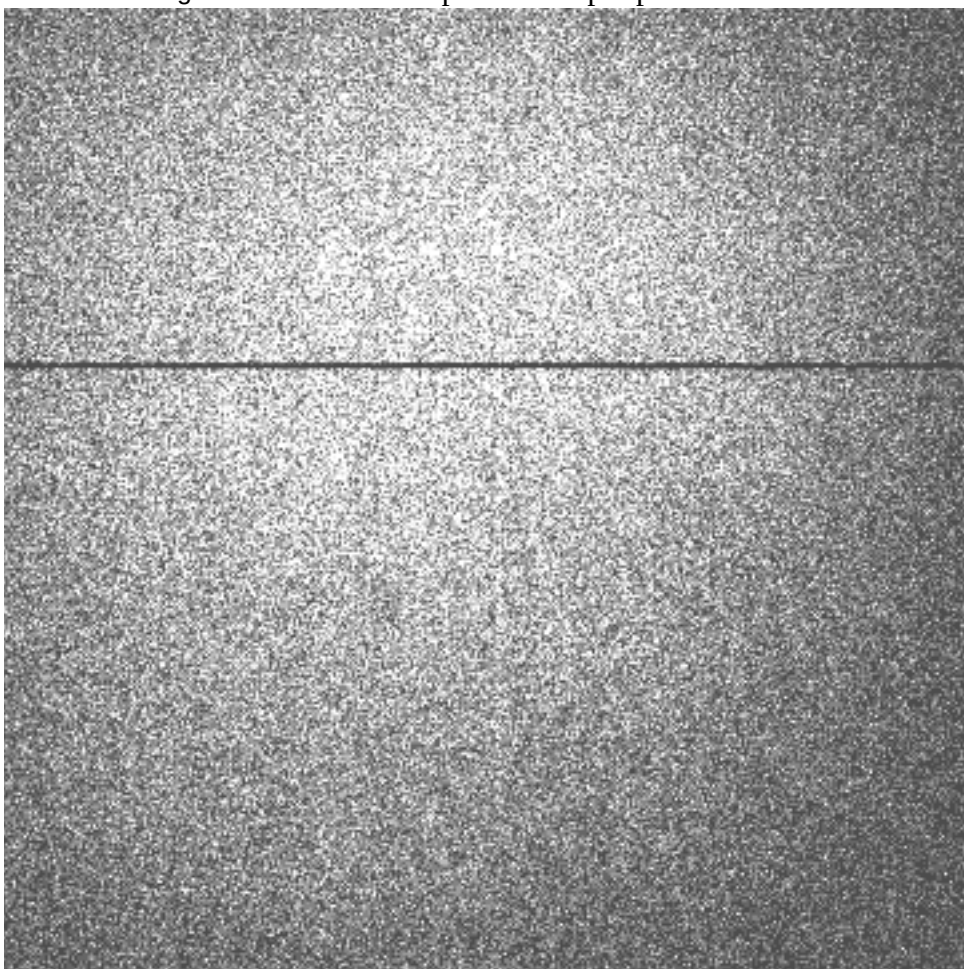

1.5.4 SBC signal-to-noise Ratio Limitations

MAMA detectors are capable of delivering signal-to-noise ratios of order 100:1 per resolution element (2×2 pixels) or even higher. Tests in orbit have demonstrated that such high S/N is possible with STIS (Kaiser et al., *PASP*, 110, 978; Gilliland, STIS ISR 1998-16). For targets observed at a fixed position on the detector, the signal-to-noise ratio is limited by systematic uncertainties in the small-scale spatial and spectral response of

the detector. The MAMA flats show a fixed pattern that is a combination of several effects including beating between the MCP array and the anode pixel array, variations in the charge-cloud structure at the anode, and low-level capacitive cross-coupling between the fine anode elements. Intrinsic pixel-to-pixel variations are of order 6% but are stable to < 1%. Photometric accuracy can be improved by averaging over flat field errors by dithering the observation (see Section 7.4).

1.5.5 SBC Flatfield

Figure 1.20: MAMA flat field. Wavelength independent P-Flat for the SBC MAMA (full frame shown).

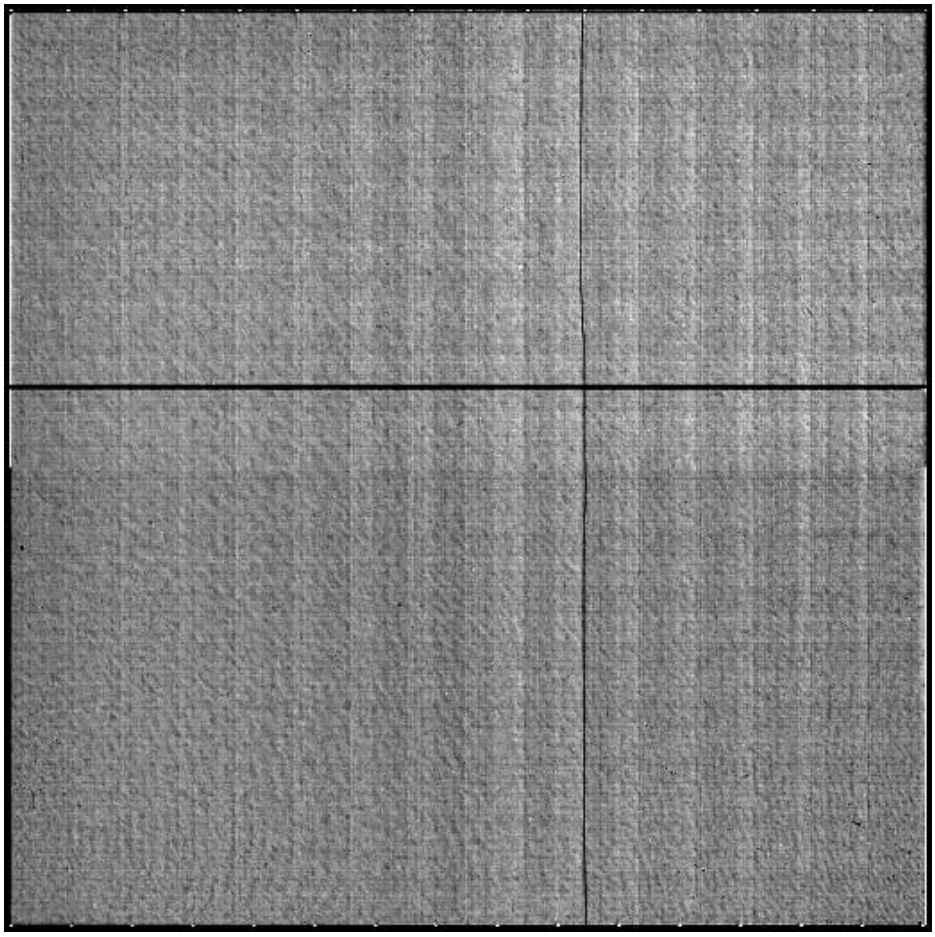

The SBC requires two types of flat fields: the "pixel-to-pixel flats" (or P-flats), which take care of the high-frequency structures in the detector sensitivity, and the "low-order flats" (or L-flats), which handle the low-frequency components. Current P-flats were derived by Bohlin & Mack (ACS ISR 2005-04) using the on-board deuterium lamp and were found to be independent of wavelength. The P-flat in Figure 1.20 shows the

effect of the disabled broken anode for rows 601 to 605 and of the shadow of the repeller wire around column 577.

Low-frequency flatfield corrections for the SBC imaging modes have been derived using multiple exposures of the globular cluster NGC6681 (Mack, et. al., ACS ISR 2005-013). Variations of 6% (full range) were found for the F115LP and F125LP filters, 8% for the F140LP and F150LP filters, and 14% for the F165LP filter. The F122M filter was not included in this analysis due to lack of sufficient data. The L-flat shows a similar general pattern in all filters, with the required correction increasing with wavelength. The L-flat analysis detected a decline in the UV sensitivity with time at a level of 2 to 4%/yr over the first 1.6 years of operation. The sensitivity appears to have leveled off after this time. A slight sensitivity loss as a function of temperature (~0.1%/degree) was also discovered. These effects were detected for the STIS FUV-MAMA detector (see STIS ISRs 2003-01 and 2004-04).

1.5.6 SBC Nonlinearity

Global

The MAMA detector begins to experience nonlinearity (photon impact rate not equal to photon count rate) at global (across the entire detector) count rates of 200,000 counts/second. The nonlinearity reaches 10% at 360,000 counts/second and can be corrected for in post-observation data processing at the price of a loss of photometric reliability. Additionally, the MAMA detector plus processing software are not able to count reliably at rates exceeding 285,000 counts/second. For this reason, and to protect the detectors, observations beyond this rate are not allowed (see Section 1.6).

Local

The MAMA detector remains linear to better than 1% up to ~22 counts/second/pixel. At higher rates, it experiences local (at a given pixel) nonlinearity. The nonlinearity effect is image dependent—that is, the nonlinearity observed at a given pixel depends on the photon rate affecting neighboring pixels. This property makes it impossible to correct reliably for the local nonlinearity in post-observation data processing. In addition, MAMA detectors are subject to damage at high local count rates (see Section 1.6).

1.6 SBC Bright-Object Limits

STScI has responsibility to ensure that the MAMA detectors are not damaged through over-illumination. Consequently, we have developed procedures and rules to protect the MAMA. We ask all potential users to share in this responsibility by reading and taking note of the information in this section, and designing observing programs which operate in the safe regime for these detectors. The safety of all proposed SBC targets and fields must be discussed in the Phase I proposal, so that their feasibility can be assessed by the TAC and STScI.

1.6.1 Overview

The SBC detector is subject to catastrophic damage at high global and local count rates, and cannot be used to observe sources which exceed the defined safety limits. The potential detector damage mechanisms include over-extraction of charge from the microchannel plates causing permanent reduction of response, ion feedback from the microchannel plates causing damage to the photocathode, and release of gas which can overpressure the tube.

To safeguard the detector, checks of the global (over the whole detector) and local (per pixel) illumination rates are automatically performed in flight for all SBC exposures. The *global illumination rate* is monitored continuously; if the global rate approaches the level where the detector can be damaged, the high voltage on the detector is automatically turned off. This event can result in the loss of all observations scheduled to be taken with that detector for the remainder of the calendar (~1 week). The *peak local illumination rate* is measured over the SBC field at the start of each new exposure. If the local rate approaches the damage level, the SBC filter wheel will be used to block the light, since there is no “shutter”. Also, all subsequent SBC exposures in the obset will be lost until a new filter is requested.

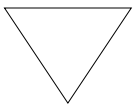

Sources that would over-illuminate the SBC detector cannot be observed. It is the responsibility of the observer to avoid specifying observations that exceed the limits described below. Please refer to Section 7.2 for more information and address this issue in your Phase I proposal.

1.6.2 Observational Limits

To ensure the safety of the SBC detector and the robustness of the observing timeline, we have established observational limits on the incident count rates. Observations which exceed the allowed limits will not be scheduled. The allowed limits are given in Table 7.3, which includes separate limits for nonvariable and irregularly-variable sources. The limits for irregular variable sources are a factor 2.5 more conservative than for sources with predictable fluxes. Predictable variables are treated as nonvariable for this purpose. Examples of sources whose variability is predictable are Cepheids or eclipsing binaries. Irregularly variable sources are, for instance, cataclysmic variables or AGN.

SBC observations of targets subject to large, unpredictable outbursts must be preceded by groundbased monitoring within the previous 24 hours, or by an HRC NUV observation a couple of orbits in advance. In the latter case, the HRC observation must be included in the Phase I orbit request.

For further information about checking for SBC bright object limits while planning your observations, please refer to Section 7.2.

CHAPTER 2:

Imaging

In this chapter . . .

2.1 Imaging Overview

ACS can be used to obtain images through a variety of optical and ultraviolet filters. When the selected ACS camera is the WFC or the HRC, the appropriate filter in one of the two filter wheels is rotated into position, and a clear aperture is automatically selected on the other filter wheel. For SBC imaging the single filter wheel is rotated to the required position. A number of apertures are defined for each ACS camera. In general, these refer to different target positions on the detector.

Table 2.1, Table 2.2, and Table 2.3 provide a complete summary of the filters available for imaging with each detector. Figures 2.1 through 2.6 show the filter transmission curves, and Figure 2.7 shows the integrated system throughputs.

The CCD filter wheels contain filters of two different sizes. Some filters (F435W, F475W, F502N, F550M, F555W, F606W, F625W, F658N, F660N, F775W, F814W, F850LP, and, G800L) are full-sized filters that can be used with both WFC and HRC. Others (F220W, F250W, F330W, F344N, F892N, POL0UV, POL60UV, POL120UV, POL0V, POL60V, POL120V, and PR200L) are smaller, giving a full unvignetted field of view when used with the HRC, but a vignetted field of view of only 72×72 arcseconds when used with the WFC. Use of the small UV filters is not supported with the WFC due to the unpredictable behavior of the silver coatings shortward of 4000 Å.

The ramp filters are designed to allow narrow or medium band imaging centered at an arbitrary wavelength. Each ramp filter is divided into three segments, of which only the middle segment may be used with the HRC. More information is available at Section 7.7.2.

Note that although the CLEAR filters are specified in the filter wheel tables, users do not need to specify these filters in their HST proposals; they are added automatically in conjunction with the desired filter in the complementary wheel. In the SBC filter wheel, every third slot (#1, 4, 7, 10) is blocked off, so that in the case of a bright object limit violation, it is only necessary to rotate the filter wheel to an adjacent slot to block the incoming light.

With either the WFC or HRC, it is possible to select a filterless observation by specifying CLEAR (this is an "available-but-unsupported" filter) as the filter name, although the image will be of degraded quality. Rough wavelengths and widths, when used with the WFC or HRC, are listed in Table 2.1 under CLEAR entries. Use of CLEAR will provide slightly degraded PSFs with the HRC and seriously degraded PSFs for the WFC. More details on PSFs with use of CLEAR are provided in ACS ISR 2003-03. Applications are expected to be rare, but a valid use could be astrometry of extremely faint targets with the HRC when color information is not required.

Table 2.1: ACS WFC/HRC filters in Filter Wheel #1.

Filter name	Central wavelength (Å)	Width (Å)	Description	Camera
CLEAR	6200	5200	Clear aperture	WFC/HRC
F555W	5346	1193	Johnson V	WFC/HRC
F775W	7764	1528	SDSS i	WFC/HRC
F625W	6318	1442	SDSS r	WFC/HRC
F550M	5580	547	Narrow V	WFC/HRC
F850LP	9445	1229	SDSS z	WFC/HRC
POL0UV	2000 to 6000	-	0˚ UV polarizer	HRC[/WFC]
POL60UV	2000 to 6000	-	60˚ UV polarizer	HRC[/WFC]
POL120UV	2000 to 6000	-	120˚ UV polarizer	HRC[/WFC]
F892N	8917	154	Methane (2%)	HRC/[WFC]
F606W	5907	2342	Broad V	WFC/HRC
F502N	5022	57	[OIII] (1%)	WFC/HRC
G800L	5800 to 11,000	-	Grism (R~100)	WFC/HRC
F658N	6584	78	Hα (1%)	WFC/HRC
F475W	4760	1458	SDSS g	WFC/HRC

[/WFC] indicates that polarizer filters, designed for the HRC field of view, induces vignetting when used with the WFC, producing a 72 by 72 arcsecond field of view.

Table 2.2: ACS WFC/HRC filters in Filter Wheel #2.

Filter name	Central wavelength (Å)	Width (Å)	Description	Camera
CLEAR	6000	5200	Clear aperture	WFC/HRC
F660N	6602	40	[NII] (1%)	WFC/HRC
F814W	8333	2511	Broad I	WFC/HRC
FR388N	3710 to 4050	2%	[OII] Ramp—middle segment	WFC/HRC
FR423N	4050 to 4420	2%	[OII] Ramp—inner segment	WFC
FR462N	4420 to 4820	2%	[OII] Ramp—outer segment	WFC
F435W	4297	1038	Johnson B	WFC/HRC
FR656N	6270 to 6850	2%	Hα Ramp—middle segment	WFC/HRC
FR716N	6850 to 7470	2%	Hα Ramp—inner segment	WFC
FR782N	7470 to 8160	2%	Hα Ramp—outer segment	WFC
POL0V	4000 to 8000	-	0˚ Visible Polarizer	HRC[/WFC]
F330W	3354	588	HRC U	HRC
POL60V	4000 to 8000	-	60˚ Visible Polarizer	HRC[/WFC]
F250W	2696	549	Near-UV broadband	HRC
POL120V	4000 to 8000	-	120˚ Visible Polarizer	HRC[/WFC]
PR200L	2000 to 4000	-	NUV Prism (R~100 @ 200 nm)	HRC
F344N	3434	60	Ne V (2%)	HRC
F220W	2228	485	Near-UV broadband	HRC
FR914M	7570 to 10,710	9%	Broad Ramp—middle segment	WFC/HRC
FR853N	8160 to 8910	2%	IR Ramp—inner segment	WFC
FR931N	8910 to 9720	2%	IR Ramp—outer segment	WFC
FR459M	3810 to 5370	9%	Broad Ramp—middle segment	WFC/HRC
FR647M	5370 to 7570	9%	Broad Ramp—inner segment	WFC
FR1016N	9720 to 10,610	2%	IR Ramp—outer segment	WFC
FR505N	4820 to 5270	2%	[OIII] Ramp—middle segment	WFC/HRC
FR551N	5270 to 5750	2%	[OIII] Ramp—inner segment	WFC
FR601N	5750 to 6270	2%	[OIII] Ramp—outer segment	WFC

[/WFC] indicates that polarizer filters, designed for the HRC field of view, induces vignetting when used with the WFC, producing a 72 by 72 arcsecond field of view.

Table 2.3: ACS SBC filter complement.

Filter name	Description
F115LP	MgF_2 (1150 Å longpass)
F125LP	CaF_2 (1250 Å longpass)
F140LP	BaF_2 (1400 Å longpass)
F150LP	Crystal quartz (1500 Å longpass)
F165LP	Fused Silica (1650 Å longpass)
F122M	Ly-α (λ = 1200 Å, Δλ = 60 Å)
PR110L	LiF Prism (R~100)
PR130L	CaF_2 Prism (R~100)

Figure 2.1: ACS broad-band filters.

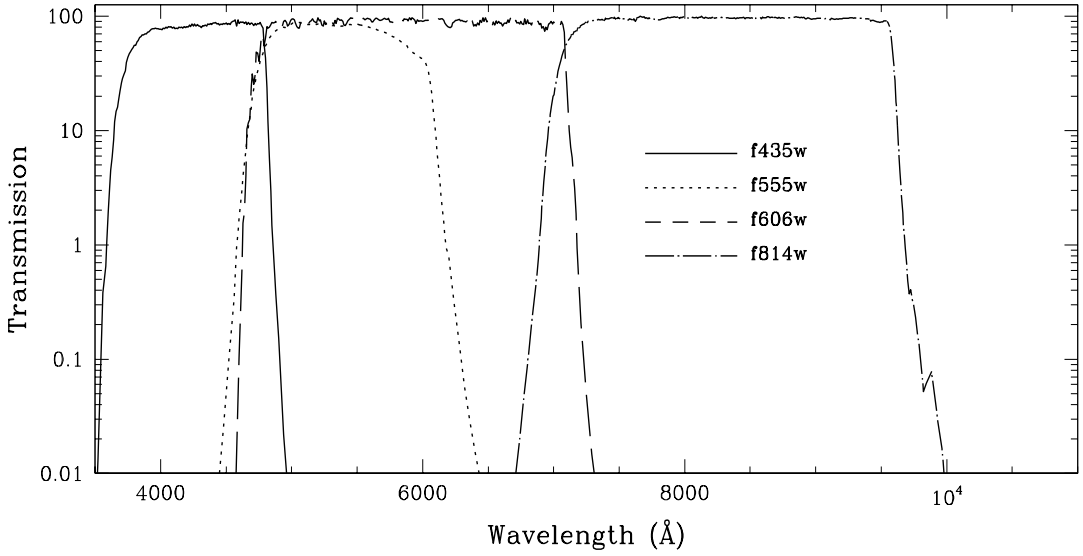

Figure 2.2: ACS SDSS filters.

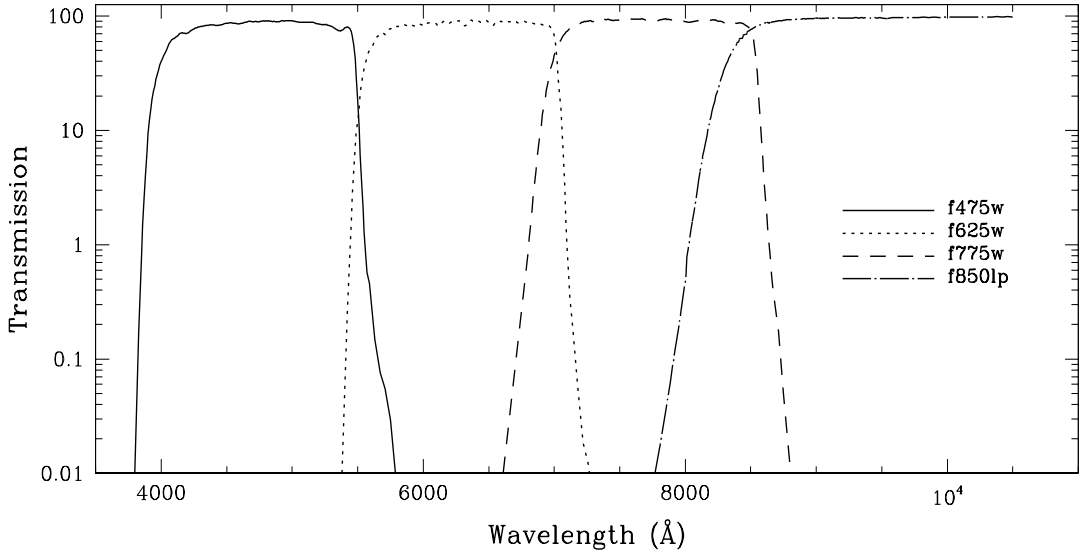

Figure 2.3: ACS UV and medium-band filters.

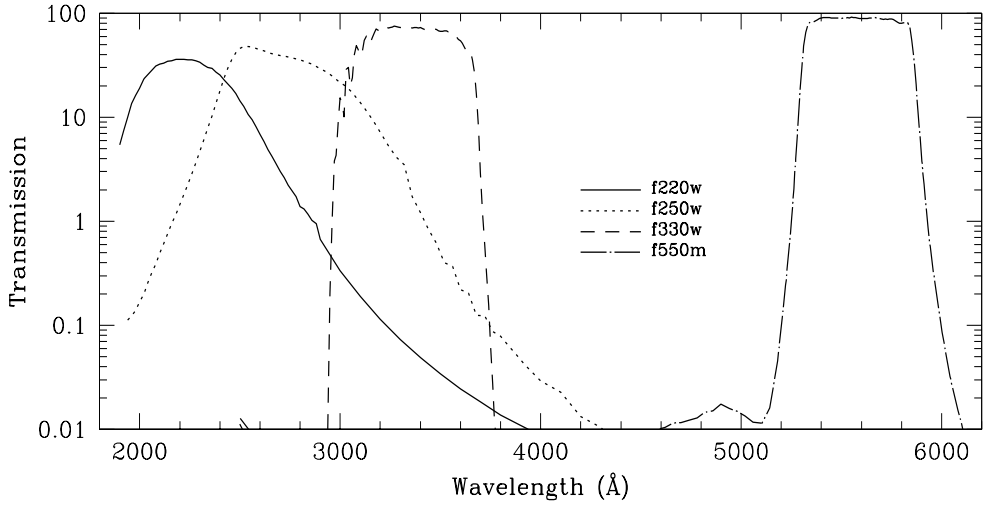

Figure 2.4: ACS narrow-band filters.

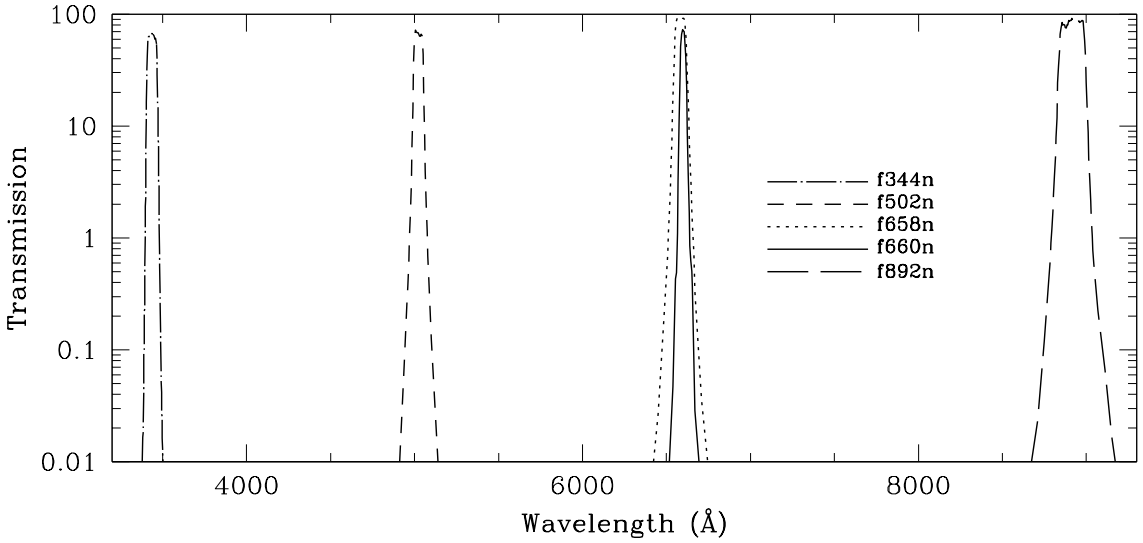

Figure 2.5: ACS SBC filters.

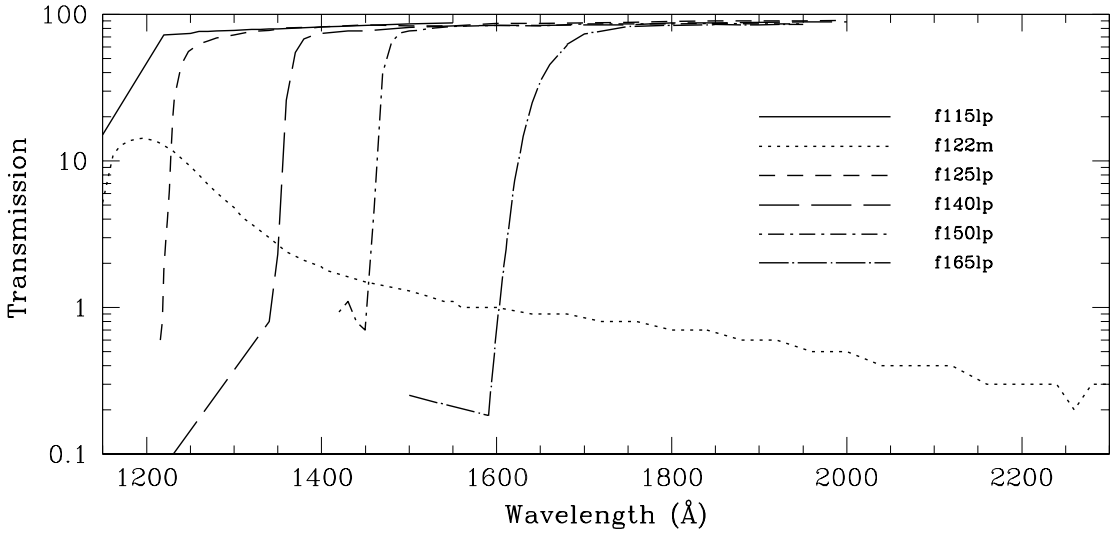

Figure 2.6: Comparison between the ACS and WFPC2 ramp filters.

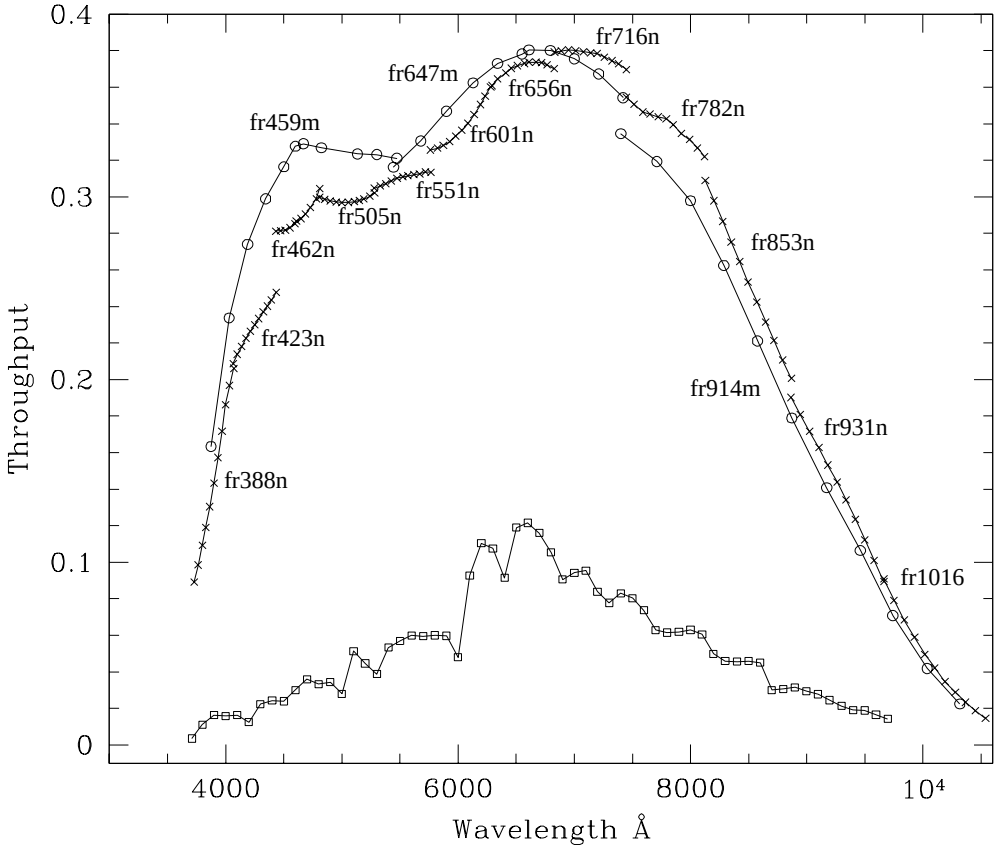

The crosses and open circles are for the ACS narrow and medium band ramps. The open squares are for the 4 WFPC2 ramps. For each of the ACS ramps the peak throughput that was calculated for eleven central wavelength values is plotted. For the WFPC2 ramps, the peak throughput calculated every 100 Å within the field of view of any of the 4 chips, and a 0∞ filter rotation angle (as mapped in Figures 3.4 and 3.5 of the WFPC2 Instrument Handbook, version 3.0), are plotted.

2.2 Important Considerations for ACS Imaging

There are a few characteristics of ACS that should be taken into account when imaging with ACS:

- The HRC and WFC filters are housed in two filter wheels shared by both cameras. As a consequence, when a filter is chosen for the primary camera, the filter used in the parallel camera is not independently selectable.
- The ACS cameras are designed to be used with a single filter, and for this reason unfiltered imaging or imaging through two filters leads to significantly degraded imaging quality (particularly in the WFC) and is not normally used except for polarization observations, or bright

target acquisitions with the HRC. The polarizer filters were designed with a zero optical thickness so that they can and should be used with another filter.

- The geometric distortion of the WFC is significant and causes the projected pixel area to vary by 9% over the field of view. This distortion affects both the photometric accuracy and the astrometric precision, and must be accounted for when the required accuracy is better than 10%.
- The ratio of in-band vs. out-of-band transmission for the ACS CCD UV filters is similar to that of WFPC2, once the two detector QE curves are taken into account (the red leak on ACS F330W is very small). This implies that the effect of filter red leaks needs to be calibrated for UV imaging of intrinsically red objects.
- The cosmic ray fluxes for HRC and WFC are comparable, respectively, to those of the STIS CCD and WFPC2. As with these instruments, typical imaging observations will need to be split or dithered for cosmic ray rejection.
- Section 1.3.5 provides further details and a recommendation that separate exposures with small dithers be used as a means of helping to remove residual hot pixels.
- The large format of the WFC requires significantly more shifts to read out data compared to STIS or WFPC2. Therefore, the impact of decreasing charge transfer efficiency will be encountered earlier. Section 1.3.7 details current expectations.
- The default GAIN setting for WFC primary observations is GAIN=2. This allows for good sampling of the readout noise and allows one to reach the full well counts of WFC. For the HRC primary observations, the default gain is GAIN=2. To sample the detector full well depth, GAIN=4 is needed, but this results in modest undersampling of the readout noise. For HRC ACQ data, the default setting is GAIN=4. Users may select the GAIN they wish to use for their ACS observations by using the GAIN optional parameter in their Phase II proposal. However, not all GAIN settings are supported (see Section 7.6).
- At wavelengths longward of ~8000 Å, internal scattering in the HRC CCD produces an extended PSF halo. This should affect only a small number of observations since the WFC camera is normally preferred at these wavelengths. The WFC CCDs include a front-side metallization that eliminates the large angle, long wavelength halo problem for $\lambda <$ 9000 Å. (For observations of red targets with the F850LP refer to Section 9.3.2).

- The ACS filter complement is not as rich as that in WFPC2. In particular, the Strömgren filter set and several narrow band filters available in WFPC2 (F375N, F390N, F437N, F469N, F487N, F588N, F631N, F656N, F673N, F953N) are not available on ACS. In general, these filters were not heavily used by the GO community. For most applications they can be replaced with the ACS medium and narrow ramps.

2.2.1 Optical Performance

Testing of the WFC and HRC cameras, following fine alignment activities on-orbit, has shown that the optical quality objectives of the cameras are met. The encircled energy values obtained from observations made in SMOV are given in Table 2.4.

Table 2.4: Encircled energy measurements for the ACS channels.

Channel	Encircled energy	
	Center of field	Edge of field
WFC at 632.8 nm in 0.25 arcseconds diameter	80.0%	79.4%
HRC at 632.8 nm in 0.25 arcseconds diameter	81.8%	81.6%
SBC at 121.6 nm in 0.10 arcseconds diameter	28%	---

2.2.2 CCD Throughput Comparison

Figure 2.7 shows the throughput of the two unfiltered ACS CCD cameras: WFC and HRC. Superposed on this plot are unfiltered WFPC2 (WF4) and the clear STIS throughputs.

2.2.3 Limiting Magnitudes

Table 2.5 contains Johnson-Cousins V magnitudes for unreddened O5 V, A0 V, and G2 V stars, generated using the Exposure Time Calculator. WFC and HRC values used the parameters CR-SPLIT=2, GAIN=2, and a 0.2 arcsecond circular aperture. For the SBC, a 0.5 arcsecond circular aperture was used. An average sky background was used in these examples. However, limiting magnitudes are sensitive to the background levels; for instance, the magnitude of an A0 V in the WFC using the F606W filter changes by 0.4 magnitudes at the background extremes.

Figure 2.7: ACS CCD system throughputs + OTA versus those of STIS and WFPC2.

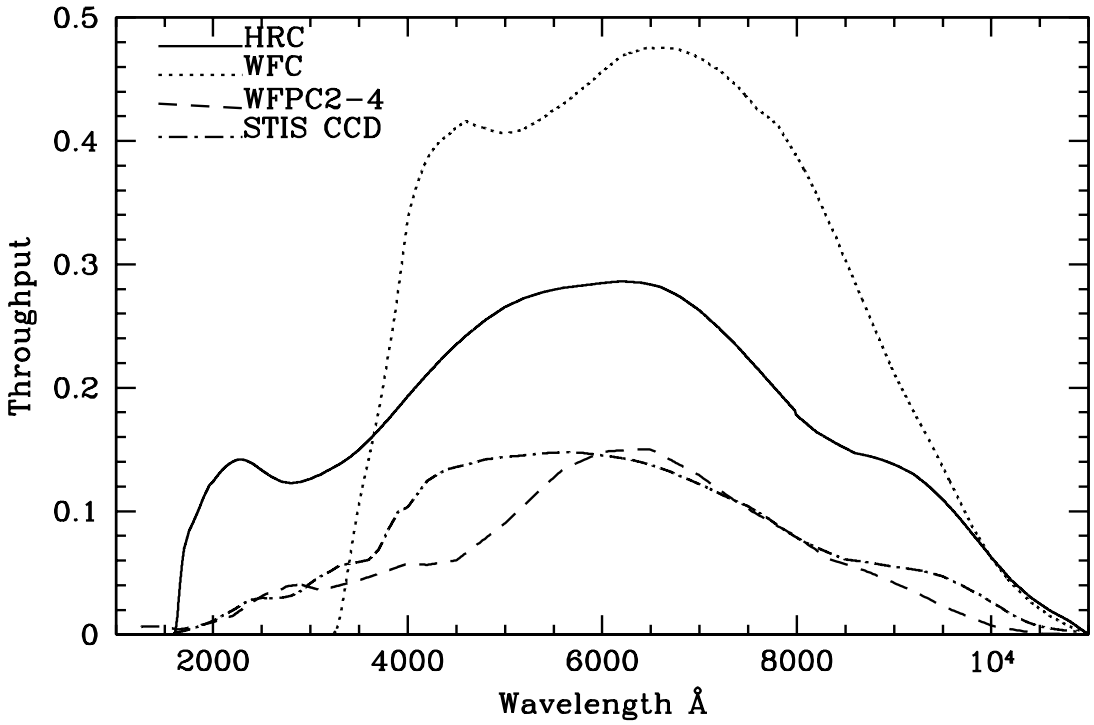

Table 2.5: V detection limits for ACS, HRC, and SBC direct imaging.

Camera	Filter	V limit (S/N = 5, exposure time = 1 hour)		
		O5 V (Kurucz model)	A0 V (Vega)	G2 V (Sun)
WFC	F606W	27.8	27.8	28.0
WFC	F814W	26.7	27.0	27.7
HRC	F330W	26.8	24.8	24.1
HRC	F606W	27.3	27.3	27.5
SBC	F125LP	27.8	23.2	13.5

2.2.4 Signal-To-Noise Ratios

In Chapter 10, we present, for each imaging mode, plots of exposure time versus magnitude to achieve a desired signal-to-noise ratio. These plots, which are referenced in the individual imaging-mode sections below, are useful for getting an idea of the exposure time you need to accomplish your scientific objectives. More accurate estimates require the use of the ACS Exposure Time Calculator (http://www.stsci.edu/hst/acs/software).

2.2.5 Saturation

Both CCD and SBC imaging observations are subject to saturation at high total accumulated counts per pixel. For the CCDs, this is due either to the depth of the full well or to the 16 bit data format. For the SBC, this is due to the 16 bit format of the buffer memory (see Section 1.3.1 and Section 1.5.2).

2.3 Wide Field Optical CCD Imaging

The Wide Field Channel of ACS was designed primarily for high throughput observations at visible wavelengths. The use of protected silver mirror coatings, the small number of reflections, and the use of a red sensitive CCD have provided the high throughput required for this camera at the expense of a 3700 Å blue cutoff. The WFC detectors are two butted 2K by 4K thinned, backside-illuminated, SITe CCDs with a red optimized coating and long-λ halo fix. The plate scale is 0.050 arcseconds per pixel, which provides a good compromise between adequately sampling the PSF and a wide field of view. The WFC PSF is critically sampled at 11,600 Å and undersampled by a factor 3 at the blue end of the WFC sensitivity range (3700 Å). We expect that it will be possible to achieve a final reconstructed FWHM of 0.100 to 0.140 arcseconds for well-dithered observations. Because the WFC PSF FWHM is largely dependent on the blurring caused by CCD charge diffusion, dithering will not be able to recover the full resolution of the optical system. See Section 7.4 for more discussion of how to use dithered observations to optimally sample the PSF.

The optical design of the camera introduces a two-component geometric distortion. The detectors themselves are at an angle with respect to the optical axis. This produces an 8% stretching of one pixel diagonal compared to the other. As a result, WFC pixels project on the sky as rhombuses rather than squares. These effects are purely geometrical and are routinely corrected in the ACS data reduction pipeline. The second component of geometric distortion is more complex. This distortion causes up to 9% variation in effective pixel area and needs to be taken into account when doing accurate photometry or astrometry as the effective area of the detector pixels varies nonlinearly with field position.

2.3.1 Filter Set

WFPC2 and Johnson-Cousins filters

All of the most commonly used WFPC2 filters are included in the ACS filter set. In addition to a medium and a broad V band filter (F550M and F606W), there is a complete Johnson-Cousins *BVI* set (F435W, F555W, F814W).

Sloan Digital Sky Survey filters

The Sloan Digital Sky Survey (SDSS) *griz* filter set (F475W, F625W, F775W, F850LP) is designed to provide high throughput for the wavelengths of interest and excellent rejection of out-of-band wavelengths. The filters were designed to provide wide, non-overlapping filter bands that cover the entire range of CCD sensitivity from blue to near-IR wavelengths.

Narrow Band filters

The Hα (F658N), [OIII] (F502N), and [NII] (F660N) narrow band filters are full-size, and can be used with both the WFC and HRC.

Ramp filters

ACS includes a complete set of ramp filters that provide full coverage of the WFC wavelength range at 2% and 9% bandwidth. Each ramp filter consists of three segments. The inner and outer filter segments can be used with the WFC only, while the middle segments can be used by both WFC and HRC. Unlike the WFPC2, where the desired wavelength is achieved by offsetting the telescope, the wavelength of ACS ramps is selected by rotating the filter while the target is positioned in one of the pre-defined apertures. The monochromatic field of view of the ramp filters is approximately 40 by 80 arcseconds. Details of how to use the ramp filters are given in Section 7.7.2.

Polarizer filters

The WFC/HRC filter wheels contain polarizers with pass directions spaced by 60°, optimized for both the UV (POL0UV, POL60UV, and POL120UV) and the visible (POL0V, POL60V, and POL120V). All the polarizer filters are sized for the HRC field of view. They induce vignetting when used with the WFC, for which the FOV will be about 72 by 72 arcseconds. More information on the use of the polarizers is given in Chapter 6.

Grism and Prism

The CCD channels also have a grism (G800L) for use with both WFC and HRC from 5500 Å to 11,000 Å, and a prism (PR200L) for use with the HRC from 1600 Å to 3500 Å. These are described more fully in Chapter 6.

2.4 High-Resolution Optical and UV Imaging

The High Resolution Channel of ACS is the prime ACS camera for near-UV imaging. HRC provides high throughput in the blue and a better sampling of the PSF than either the WFC or other CCD cameras on HST. The HRC pixel size critically samples the PSF at 6300 Å and is undersampled by a factor 3.0 at the blue end of its sensitivity range (2000 Å). With this capability, the HRC functionally replaces the Faint Object Camera as the instrument able to critically sample the PSF in the V band. For this reason, most of the usage of HRC will be for UV and blue imaging. HRC can also be convenient for imaging in the red when the PSF sampling is important. As an example, better PSF sampling is probably important for accurate stellar photometry in crowded fields. We expect that the photometric accuracy achievable by the HRC will be higher than that achievable with the WFC. Well-dithered observations with the HRC should lead to a reconstructed PSF FWHM of 0.03 arcsec at ~4000 Å, increasing towards longer wavelengths. HRC also includes a coronagraph that is discussed in Chapter 6. The HRC CCD presents a long wavelength halo problem similar to the STIS CCD since the front-side metallization correcting the halo problem for the WFC CCDs was implemented only after the HRC CCD had been procured. Although most of the HRC imaging is likely to occur in the UV, users should be cautioned to take into account the effects of the long wavelength halo when using the HRC in combination with near-IR filters (See Section 2.6.5).

2.4.1 Filter Set

The HRC-specific filters are mostly UV and blue. The set includes UV and visible polarizers (discussed in Chapter 6), a prism (PR200L, discussed in Chapter 6), three medium-broad UV filters (F330W, F250W, and F220W) and two narrow band filters (F344N and F892N). Use of the UV filters with the WFC is not supported because of the uncertainty of the WFC silver coating transmission below 4000 Å.

All broad, medium and narrow band WFC filters can be used with the HRC whenever a better PSF sampling is required. In general, the throughput of WFC is higher than that of HRC where their sensitivity overlaps. Only some of the WFC ramp segments can be used with the HRC since only the middle segment overlaps with the HRC FOV. In particular, HRC can use the FR459M and FR914M broad ramps, and the FR505N [OIII], FR388N [OII], and FR656N (Hα) narrow ramps.

2.4.2 Multiple Electron Events

Like the STIS CCD but unlike WFPC2, the HRC CCD is directly sensitive to UV photons and for this reason is much more effective in detecting them. However, whenever a detector has non-negligible sensitivity over more than a factor two in wavelength, it becomes energetically possible for a UV photon to generate more than one electron and be counted more than once. This effect has been seen for STIS and also during the ground testing of the HRC detector. The effect is only important shortward of 3200 Å, and reaches a magnitude of approximately 1.7 e^-/photon at 2000 Å. Multiple counting of photons has to be taken into account when estimating the detector QE and the noise level of a UV observation since multiple photons cause a distortion in the Poisson distribution of electrons.

2.4.3 Red Leaks

When designing a UV filter, a high suppression of off-band transmission, particularly in the red, has to be traded with overall in-band transmission. The very high blue quantum efficiency of the HRC compared to WFPC2 makes it possible to obtain an overall red leak suppression comparable to that of the WFPC2 while using much higher transmission filters. In Cycle 14 we obtained new calibration data to check the impact of red leaks on observations. The results are described in ACS ISR 2007-003. In Table 5.6 we show the ratio of in-band versus total flux for a few UV and blue HRC filters, where the cutoff point between in-band and out-of-band flux is defined as the filter's 1% transmission point. The same ratio is also listed for the equivalent filters in WFPC2. Correction factors for different stellar spectral types and non-stellar spectra can be found in the ISR. Clearly, red leaks are not a problem for F330W, F435W, and F475W. Red leaks are more important for F250W and F220W. In particular, accurate UV photometry of objects with the spectrum of an M star will require correction for the redleak in F250W and will be essentially impossible in F220W. For the latter filter a red leak correction will also be necessary for K and G stars.

Table 2.6: In-band flux as a percentage of the total flux.

Stellar type	WFPC2 F218W	HRC F220W	WFPC2 F255W	HRC F250W	WFPC2 F300W	HRC F330W	WFPC2 F439W	HRC F435W	WFPC2 F450W	HRC F475W
O5 V	99.8	99.6	99.6	99.7	99.9	99.9	99.9	99.9	99.9	99.9
B1 V	99.7	99.6	99.6	99.7	99.9	99.9	99.9	99.9	99.9	99.9
A1 V	99.4	98.8	99.2	99.0	99.2	99.9	99.9	99.9	99.9	99.9
F0 V	98.5	97.0	98.8	98.3	98.8	99.9	99.9	99.9	99.9	99.9
G2 V	92.5	88.7	97.4	97.1	97.4	99.9	99.9	99.9	99.8	99.9
K0 V	71.7	60.6	95.0	95.2	95.0	99.9	99.9	99.9	99.8	99.9
M2 V	0.03	1.5	45.5	62.4	45.4	99.9	99.9	99.9	99.6	99.9

2.5 Ultraviolet Imaging with the SBC

The Solar Blind Channel is the ACS camera optimized for UV imaging. The SBC uses the same optical train as the HRC and is comparable in performance to the FUV MAMA of STIS. The use of the repeller wire increases the quantum efficiency of the detector by ~30%, but adds a halo to the PSF. Bright object limits are discussed in detail in Section 7.2.

2.5.1 Filter Set

Several filters are available for use with the SBC, including a Lyman α narrow band filter (F122M), a long pass quartz filter (F150LP), MgF_2 filter (F115LP), and a CaF_2 filter (F125LP). The SBC also includes two additional long pass filters (F140LP and F165LP) as well as prisms (discussed in Chapter 6). A list of filters is given in Table 2.3

2.5.2 Red Leaks

The visible light rejection of the SBC is excellent, but users should be aware that stars of solar type or later will have a significant fraction of the detected flux coming from outside the nominal wavelength range of the detector. This is discussed in greater detail in Section 4.4.2.

Table 2.7: Visible-light rejection of the SBC F115LP imaging mode.

Stellar type	Percentage of all detected photons which have λ < 1800 Å	Percentage of all detected photons which have λ < 3000 Å
O5	99.5	100
B1 V	99.4	100
A0 V	98.1	100
G0 V	72.7	99.8
K0 V	35.1	94.4

2.5.3 SBC Imaging Filter Shifts

The SBC focal surface, like that of the HRC, is tilted significantly with respect to the chief ray. Because the MAMA detector is a STIS spare, its window is approximately parallel to the MCP surface and the whole detector must tilt to achieve good focus over the field. Because the window is therefore tilted, "lateral color" is introduced, which would result in dispersion-induced degradation of the PSF, so the filters are canted in the opposite direction to that of the window to ameliorate the color. The filter thickness is matched to the mean index of refraction over its bandpass to maintain focus. These result in unavoidable image location offsets between filters. In contrast, the WFC and HRC filters and windows are normal to the chief ray and the detector surfaces are tilted within their housings to match the focal surface tilt. In Table 2.8, we list the shifts for each SBC imaging filter with respect to the F115LP filter. No pointing compensations are made for these offsets.

Table 2.8: Shifts between SBC imaging filters.

Spectral Element	Offset (pixels) in the x,y directions
F115LP	0,0
F122M	0,0
F125LP	-5,15
F140LP	-7,21
F150LP	-3,11
F165LP	-4,12

2.6 ACS Point Spread Functions

The ACS point spread function has been studied in ground test measurements, and by using on-orbit data and models generated by the **Tiny TIM** software (http://www.stsci.edu/software/tinytim/tinytim.html) developed by J. Krist and R. Hook. As with other HST instruments, the ACS point spread function is affected by both optical aberrations and geometric distortions. Point sources imaged with WFC and HRC experience blurring due to charge diffusion into adjacent pixels because of CCD subpixel variations, which reduces the limiting magnitudes that can be reached by WFC/HRC. The SBC PSF and the long-wavelength HRC PSF are also affected by a halo produced by the detectors themselves.

2.6.1 CCD Pixel Response Function

The sharpness of the CCD PSF is somewhat degraded by charge diffusion into adjacent pixels. The effect is usually described in terms of the pixel response function (PRF), which gives the distribution of flux from within the pixel into adjacent pixels. Charge diffusion results in ~0.5 magnitude loss in the WFC limiting magnitude at short wavelengths (the worst case). At longer wavelengths and at all wavelengths for the HRC the reduction in the limiting magnitude is ~0.2 magnitudes or less. Due to variations in the CCD thickness, charge diffusion is not constant over the field of view. At different wavelengths, the CCD pixel response functions can be represented by the following kernels (for the center of the field):

Figure 2.8: Kernels representing CCD pixel functions for HRC and WFC.

$$K_{HRC} = \begin{bmatrix} 0.02 & 0.07 & 0.02 \\ 0.07 & 0.64 & 0.07 \\ 0.02 & 0.07 & 0.02 \end{bmatrix}, \quad K_{WFC} = \begin{bmatrix} 0.04 & 0.11 & 0.04 \\ 0.11 & 0.40 & 0.11 \\ 0.04 & 0.11 & 0.04 \end{bmatrix}$$

at λ = 4000 Å,

$$K_{HRC} = \begin{bmatrix} 0.02 & 0.06 & 0.02 \\ 0.06 & 0.68 & 0.06 \\ 0.02 & 0.06 & 0.02 \end{bmatrix}, \quad K_{WFC} = \begin{bmatrix} 0.03 & 0.10 & 0.03 \\ 0.10 & 0.48 & 0.10 \\ 0.03 & 0.10 & 0.03 \end{bmatrix}$$

at λ = 5500 Å, and

$$K_{HRC} = \begin{bmatrix} 0.02 & 0.04 & 0.02 \\ 0.04 & 0.76 & 0.04 \\ 0.02 & 0.04 & 0.02 \end{bmatrix}, \quad K_{WFC} = \begin{bmatrix} 0.02 & 0.07 & 0.02 \\ 0.07 & 0.64 & 0.07 \\ 0.02 & 0.07 & 0.02 \end{bmatrix}$$

at $\lambda = 8000$ Å.

More details on ACS CCD charge diffusion are given in ACS ISR 2006-01. For details on CTE-induced photometric losses for ACS/WFC and techniques to correct for them, see ACS ISR 2006-01.

2.6.2 Model PSFs

Table 2.9 and Table 2.10 give ACS model PSFs in the central 5×5 pixel region in two wavelength bands (filters). Numbers listed are the fraction of the total energy received in each pixel. The models have been generated using **Tiny TIM**, taking into account the HST optical aberrations and obscurations as well as the CCD pixel response function. Field dependent geometrical distortions are included. The real PSF will also differ from the model because of the jitter in the HST pointing, HST focus variation (focus breathing), and other instrumental effects, some of which are briefly discussed below. For further details on the PSF variations and an effective procedure to model them, see ACS ISR 2006-01. The SBC PSF is shown Figure 2.10.

Table 2.9: Model ACS CCD PSFs.

WFC model PSF, filter F435W					**WFC model PSF, filter F814W**				
0.00	0.01	0.01	0.01	0.00	0.01	0.01	0.02	0.01	0.01
0.01	0.04	0.07	0.05	0.02	0.01	0.03	0.07	0.03	0.02
0.02	0.08	0.17	0.08	0.02	0.02	0.07	0.18	0.07	0.02
0.01	0.04	0.08	0.04	0.01	0.01	0.03	0.07	0.03	0.01
0.00	0.01	0.02	0.01	0.00	0.01	0.02	0.02	0.01	0.00
HRC model PSF, filter F435W					**HRC model PSF, filter F814W**				
0.01	0.01	0.01	0.01	0.01	0.00	0.01	0.02	0.01	0.00
0.02	0.03	0.06	0.03	0.01	0.01	0.04	0.05	0.04	0.01
0.01	0.06	0.16	0.06	0.01	0.02	0.05	0.08	0.05	0.02
0.01	0.03	0.07	0.03	0.01	0.01	0.04	0.05	0.04	0.01
0.01	0.02	0.01	0.01	0.01	0.00	0.01	0.02	0.01	0.00

Table 2.10: Model ACS SBC PSFs.

SBC PSF at 120 nm					SBC PSF at 160 nm				
<0.01	0.01	0.01	0.01	<0.01	<0.01	<0.01	<0.01	<0.01	<0.01
0.01	0.02	0.03	0.02	0.01	<0.01	0.02	0.04	0.02	<0.01
0.01	0.03	0.15	0.03	0.01	<0.01	0.04	0.20	0.04	<0.01
0.01	0.02	0.03	0.02	0.01	<0.01	0.02	0.04	0.02	<0.01
<0.01	0.01	0.01	0.01	<0.01	<0.01	<0.01	<0.01	<0.01	<0.01

2.6.3 Encircled Energy

In general, the ACS channels encircled energy distribution has been found to be within the original instrument specifications. Figure 2.9 and Figure 2.10 show the ACS encircled energy curves derived from on-orbit images. Tabulated values of the encircled energy for most filters are available in Sirianni et al. (2005PASP 117.1049).

2.6.4 Geometric Distortions

Geometric distortions produce a significant impact on the shape of the PSF in all three of the ACS channels, as can readily be seen in Figure 2.11 and Figure 2.12, which display WFC and HRC PSF images. The log stretch enhances the spider diffraction patterns, which the distortion renders non-perpendicular, and the outer Airy rings, which appear elliptical. The distortion owes primarily to the tilt of the focal surface to the chief ray at the large OTA field angles of the ACS apertures. The linear, field-independent approximation for the WFC produces a difference in plate scale of about 8% between the two diagonals of the field and, in the HRC and SBC, about a 16.5% difference in scale between orthogonal directions rotated about 20° from the aperture edges. Field-dependent distortions, measured as actual vs. predicted distances from field center, amount to about 2% peak in the WFC and about 1% in the HRC and SBC.

The distortions render the pixels, as projected on the sky, trapezoidal in shape and their area varies over the field by about 19% and 3.5% in the WFC and HRC/SBC, respectively. These variations have significant ramifications concerning appropriate techniques for flat-fielding and photometric calibration, especially when complicated by resampling in order to combine dithered image sets. Related issues are the manner in which the halation effects of the HRC and SBC detectors are removed and the treatment of spectra from the prisms and grism, which are not subject to the same distortion effects.

More details concerning geometric distortions in ACS can be found in ACS ISR 2002-02 and ACS ISR 2004-15. An introduction to ***calacs***, and to ***multidrizzle*** which applies corrections for geometric distortion, is available on-line at:

`http://www.stsci.edu/hst/acs/analysis/multidrizzle.`

Figure 2.9: Encircled energy for the CCD channels.

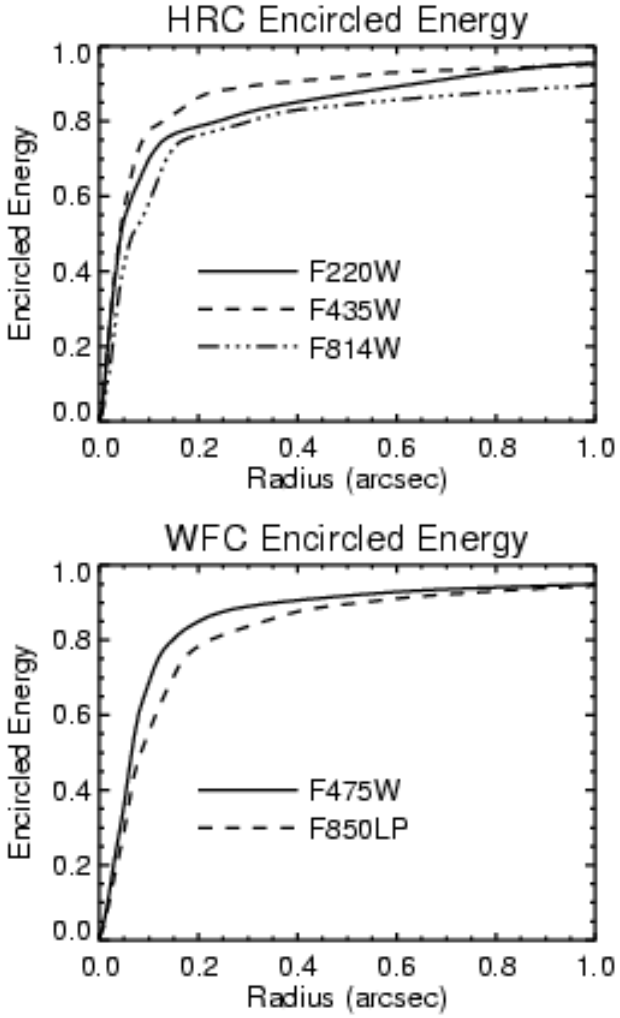

Figure 2.10: Encircled energy for the SBC.

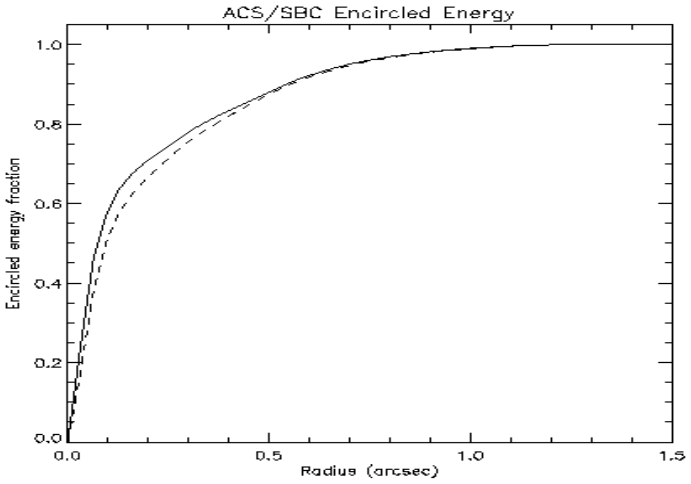

Figure 2.11: ACS WFC PSF - F625W.

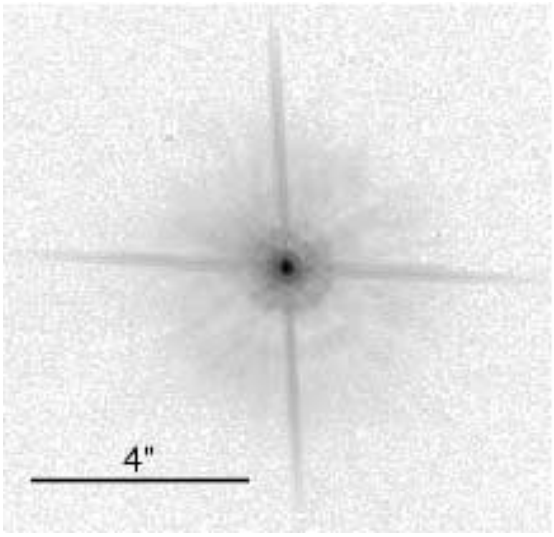

Figure 2.12: ACS HRC PSF - F625W.

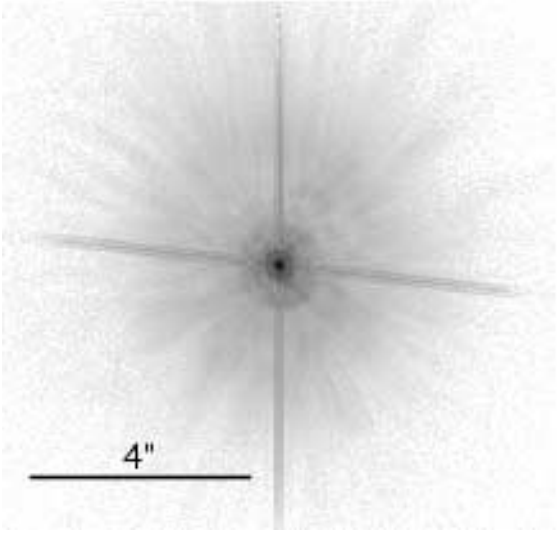

2.6.5 PSFs at Red Wavelengths and the UV

The CCDs used in the HRC and WFC suffer from a halo that is caused by very red photons passing through the device and being scattered back into the detector by the mounting substrate. This creates a large halo in HRC images beyond 7000 Å and WFC images past 9000 Å. At 8000 Å in the HRC, the halo contains about 10% of the light. At 10,000 Å, it contains about 30% and increases the surface brightness of the PSF wings by over an order of magnitude, overwhelming the PSF diffraction rings and spikes. A discussion of this may be found in Gilliland & Riess, (2002) *HST Calibration Workshop* at:

`http://www.stsci.edu/hst/HST_overview/documents/calworkshop/workshop2002/CW2002_Papers/CW02_gilliland.`

In the F850LP filter, in particular, extremely red stars show a progressive loss of flux in small to moderate sized apertures as a function of color. A paper by Sirianni et al. (2005, astroph/0507614) is available at:

`http://adcam.pha.jhu.edu/instrument/photometry/sirianni.pdf`

See also Bohlin ACS ISR 2007-06. These papers provide a detailed recipe to correct for this effect. This halo effect is only partially treated by the Exposure Time Calculator. Observers can use ***synphot*** (see Section 9.3.2) to accurately calculate the photometry of red sources in the SDSS z-filter.

Long wavelength photons that pass through the CCD can also be scattered by the electrode structure on the back side of the device and will create two spikes that extend roughly parallel to the x-axis. These spikes are seen at wavelengths longer than 9500 Å in both the HRC and WFC (see Figure 2.13 and Figure 2.14).

Figure 2.13: ACS WFC PSFs (10" x10"). FR914M images are saturated.

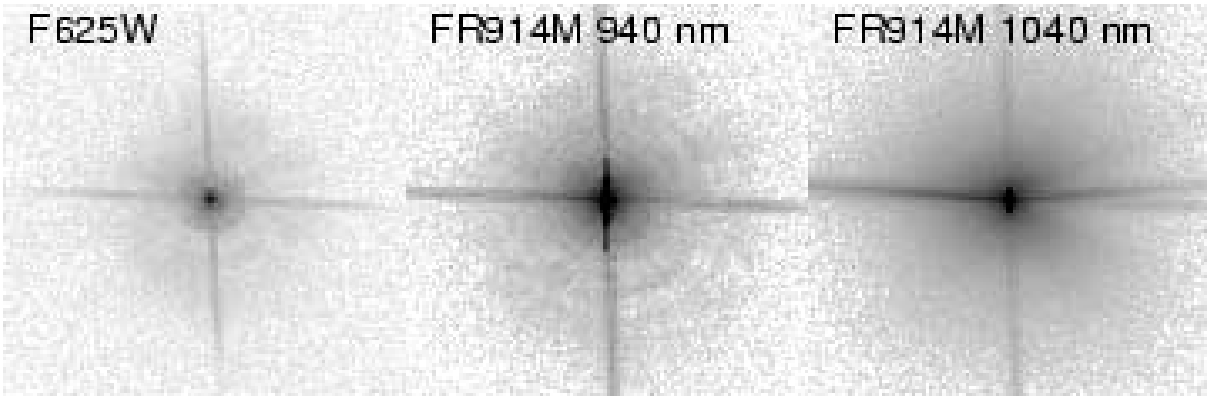

Figure 2.14: ACS HRC PSFs (3.25" x3.25").

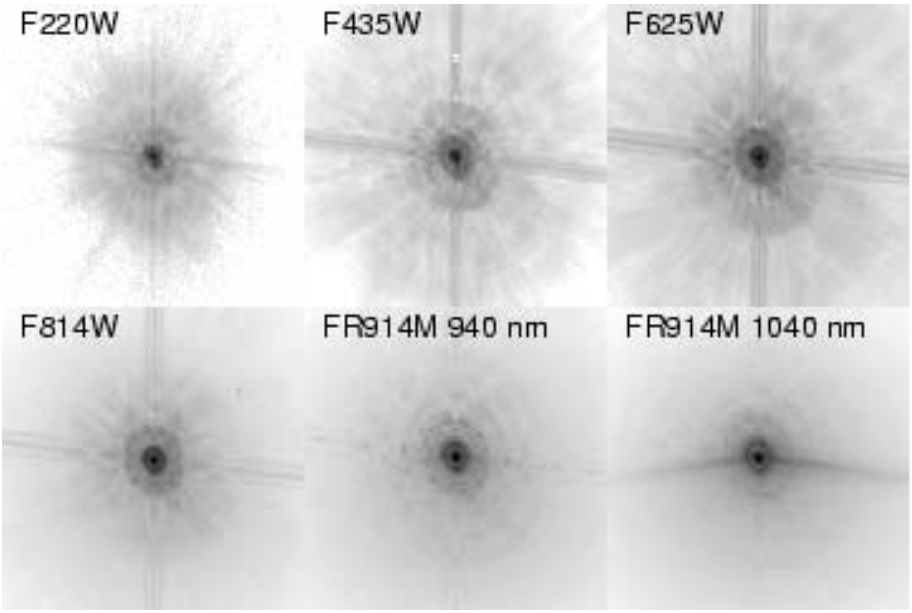

In the UV the core of the PSF becomes rather asymmetrical due to midfrequency optical surface errors. In the SBC, a halo is created by charge migration at the microchannel plate surface. This effect, seen previously in STIS MAMA images, broadens the PSF core and redistributes a small portion of flux into a broad halo that can be approximated by a Gaussian with FWHM ~20 pixels. The peak flux for a point source centered on a pixel is reduced by 30% to 40% depending on wavelength.

The encircled energy curves presented in this handbook and incorporated into the ETC include all of the scattering effects discussed here.

2.6.6 Residual Aberrations

Residual aberration levels at the center of the field in each camera are 1/30 wave (HRC) and 1/20 wave (WFC) rms at 5500Å (excluding defocus). Coma and astigmatism are minimized at the field center of each camera. The ACS PSF varies far less over the field of view than those of WFPC2 and STIS. WFPC2 especially suffers from a variable obscuration pattern that significantly alters the PSF structure depending on field position. Lacking the additional obscurations present in WFPC2, ACS PSF variations are instead due to changes in aberrations and charge diffusion.

At the extreme corners of the WFC field, increased astigmatism slightly elongates the PSF core. The axis of elongation rotates by 90° if the system passes through focus due to breathing. This may affect ellipticity measurements of small galaxies with bright cores at the field edges. Focus

variations in the WFC, which alter the amount of light in the peak, are largely due to detector surface height irregularities and amount to the equivalent of 5 microns of breathing (1/18 wave rms). The largest focus offset is along the gap between the two CCDs. Variations in the width of the PSF core are dominated by changes in CCD charge diffusion, which is dependent on the thickness of the detector (12 to 17 microns for the WFC). The PSF FWHM in F550M, for example, can vary by 20% (0.10 to 0.13 arcseconds) over the field.

The PSFs in the HRC and SBC are reasonably constant over their fields. The HRC FWHM is 0.060 to 0.073 arcseconds in F550M. More details on ACS PSF field variations are provided in ACS ISR 2003-06. The Tiny Tim PSF simulator includes field dependent aberrations and charge diffusion and may be used to estimate the impact of these variations.

A

B

C

D

E

F

G

H

I

L

M

P

Q

R

S

T

W